Microfabrication of acoustic cavities

Master Thesis

Jozef Cornelis Paulus Bus
jozbus@student.ethz.ch

Hybrid Quantum Systems group
Departement of Physics, D-PHYS
ETH Zürich

Supervisor:
Maxwell Drimmer

Professor:
Dr. Yiwen Chu

July 9, 2023

Abstract

Circuit quantum acoustodynamics (cQAD) utilises hybrid electromechanical systems to study the quanta of mechanics, phonons, and their interaction with quanta of light, photons. In this field, acoustic resonators are coherently coupled to superconducting circuits to explore the single-phonon regime. Here, we focus on the $\hbar$BAR [1], a hybrid device that consists of a transmon qubit that is piezoelectrically coupled to a high-frequency bulk acoustic wave resonator (HBAR). In this work, we present novel fabrication methods and designs of HBARs for cQAD. We focus on three HBAR variations. Firstly, sapphire devices with a novel aluminium nitride thin film and a plano-convex geometry. For this thin film, a new etching recipe has been developed to ensure sufficiently smooth surfaces. Six of these devices were measured in a dilution refrigerator at millikelvin temperatures. Some of them support phonon modes with extended lifetimes compared to previous devices. One specific device demonstrated exceptionally long-lived phonon modes, including one with $T_1 = 0.27 \pm 0.01$ ms, which is approximately a threefold enhancement compared to earlier HBARs with a similar plano-convex geometry [2]. Secondly, we considered HBAR devices with identical geometry but with an additional aluminium electrode between the aluminium nitride piezoelectric and the sapphire crystal. The electrode is employed to enhance the unidirectionality of the electric field through the piezoelectric. This could allow for more selective electromechanical coupling and mitigation of phonon radiation. Simulations were performed and devices were fabricated. Lastly, foundational work has been conducted towards developing double-sided HBARs, a convex-convex HBAR variant that divides the tasks of electromechanical coupling and phonon confinement between the piezoelectric and crystal faces, respectively. Concrete geometries and a preliminary fabrication workflow utilising direct-write greyscale lithography are proposed.

Contents

Introduction

1.1. Circuit quantum acoustodynamics (cQAD)

Circuit quantum acoustodynamics (cQAD) is the subfield in quantum physics that studies phonons, particles of sound, through the coherent interaction with a superconducting circuit [3]. By coupling acoustic cavities to an artificial atom one can investigate the relatively unexplored single-phonon regime[1, 2, 4].

Through this interaction, many parallels can be drawn to photonic systems as studied in cavity quantum electrodynamics (CQED) and circuit quantum electrodynamics (cQED). However, acoustic resonators also have various appealing characteristics that distinguish them, including the ability to support compact long-lived modes and the ability to couple to various physical systems [1, 5].

Several phononic systems have been proposed and implemented for cQAD, including high-overtone bulk acoustic wave resonators (HBARs) [1, 2, 5–7], surface acoustic waves (SAWs) [8, 9], and phononic crystal defects [10]. These systems are typically operated at millikelvin temperatures that allow them to be cooled to near the quantum ground state.

Due to the attractive features of acoustic systems, the field of cQAD also finds applications in areas like wavelength conversion [5, 11, 12], metrology [9], and quantum memories [13]. The ability to couple mechanical systems to both microwave and optical photons opens up venues to perform microwave-to-optical transduction [5]. Especially in the field of quantum computation, transduction and compact quantum memories could have profound technical utilisation.

Towards these applications, the field still needs to overcome several hurdles. These include extending the qubit and phonon coherence times while also increasing the coupling rate between the superconducting and the acoustic system. In piezoelectrically coupled systems particularly, qubit lifetimes are limiting the applicability of the hybrid system. Unintended coupling to different acoustic modes mediated by the piezoelectric is believed to be detrimental to the qubit lifetimes [14]. Negating these losses and extending the lifetimes and operation rates will e.g. enable the application of quantum error correction on the quantum information stored in the acoustic modes. Moreover, bosonic quantum information processing can be explored with encodings like the cat [6, 15, 16] and GKP [17] codes.

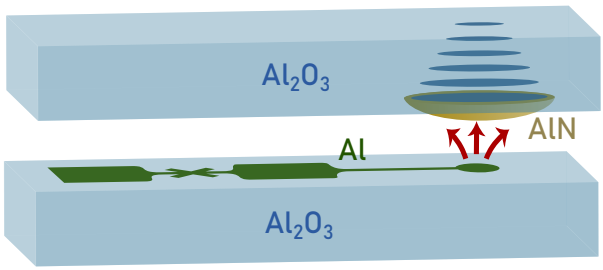

Figure 1.1: **Illustration of an $\hbar$BAR device.** The device consists of a high-overtone bulk acoustic resonator (HBAR) chip (top) that is flip-chip bonded [18] to a transmon chip. The aluminium transmon, also referred to as the antennamon, has an antenna extending from one of the capacitive pads. The plano-convex HBAR is made of a pristine sapphire (Al_2O_3) crystal and a aluminium nitride (AlN) piezoelectric dome. The dome is employed for both phonon confinement and electromechanical transduction, exchanging energy between the electrical and acoustic systems by converting strain to electric field and vice versa. For illustrative simplicity, the spacers and adhesive attaching the acoustic chip to the electrical chip are omitted. Figure adapted from [4].

In this work, we will be concerned with the design and fabrication of high-overtone acoustic resonators for $\hbar$BARs [1], hybrid devices consisting of a mechanical resonator and a superconducting transmon qubit. The two systems are fabricated on separate chips and flip-chip bonded to form the $\hbar$BAR, as shown in Figure 1.1.

1.2. Hamiltonian

We now briefly introduce the Hamiltonian that describes the $\hbar$BAR device for theoretical context. For more elaborate discussions we refer to [3, 19, 20]. The system under consideration is a hybrid device, constituting of electrical and mechanical components. To couple these two, we use a piezoelectric material that converts mechanical stress into electrical energy, and vice versa. The Hamiltonian of the combined system is [19]

$$H = \sum_{\eta} H_\eta + H_q + H_{\text{int}} \tag{1.1}$$

where we sum over the set of acoustic modes $\{\eta\}_\eta$, q designates the transmon qubit, and H_{int} describes the coupling between the two mediated by the piezoelectric. More concretely, we can approximate these terms as

$$H_\eta = \hbar\omega_\eta a_\eta^\dagger a_\eta, \tag{1.2}$$

$$H_q = \hbar\omega_q q^\dagger q - \frac{E_C}{2}(q^\dagger)^2 q^2, \tag{1.3}$$

and

$$H_{\text{int}} = \hbar \sum_{\eta} g_\eta (q^\dagger a_\eta + q a_\eta^\dagger), \tag{1.4}$$

where a_η and $a_\eta^\dagger$ are the annihilation and creation operators of the mechanical mode η, q and $q^\dagger$ are the transmon qubit operators, E_C is the charging energy of the transmon qubit, and g_η is the coupling rate between the transmon and the acoustic mode η. Here, we approximated the transmon Hamiltonian H_q to second order and the interaction term is derived from [3]

$$\tilde{H}_{\text{int}} = -\int \overleftrightarrow{\sigma}\,(\vec{r})\,\overleftrightarrow{\mathrm{S}}\,(\vec{r})\,\mathrm{d}V, \tag{1.5}$$

where $\overleftrightarrow{\sigma}(\vec{r})$ is the stress tensor, and $\overleftrightarrow{S}_\eta$ is the strain of the phonon mode η. The coupling rate g_η can be estimated by quantising the fields and equating (1.5) to the Jaynes-Cummings Hamiltonian interaction term [3]

$$g_\eta = \int \overleftrightarrow{c} \cdot \overleftrightarrow{d} \cdot \vec{E} \cdot \overleftrightarrow{S}_\eta \, dV \tag{1.6}$$

where $\overleftrightarrow{d}$ is the piezoelectric tensor that relates the strain to the electric field. This depends on the properties of the piezoelectric, such as the crystal orientation. It is a third-order tensor, but in the case of c-axis oriented aluminium nitride, we can approximate it as

$$\overleftrightarrow{d} = \begin{cases} d_{33}\, \overleftrightarrow{e}_{33} & \text{inside piezoelectric} \\ 0 & \text{outside piezoelectric} \end{cases} \tag{1.7}$$

where $\overleftrightarrow{e}_{33}$ is the unit tensor with only one non-zero element located in the third row and third column. When only considering the dominant longitudinal tensor components we find the expression [3]

$$\hbar g = c_{33} \int d_{33}(\vec{x}) \cdot E(\vec{r}) \cdot S(\vec{r}) \, dV \tag{1.8}$$

where $E \equiv E_3$, $\sigma \equiv \sigma_{33}$, $S \equiv S_{33}$ are the components normal to the substrate surface, denoted by the subscript 3. In this work, we will pay particular attention to the coherence times of the acoustic mode η and its coupling rate g_η.

This thesis is structured in the following manner. We commence with Chapter 2, where the microfabrication process of the acoustic devices is presented. Following this, Chapter 3 discusses the fabrication and measurement results of HBAR devices using the novel aluminium nitride material, paying particular attention to the developed etch recipe. Subsequently, Chapter 4 details simulations and fabrication of the electrode HBAR, whilst Chapter 5 focuses on the double-sided HBAR. Our concluding remarks are presented in Chapter 6, followed by an outlook provided in Chapter 7.

Microfabrication of high-overtone acoustic resonators

To experimentally probe the quantum mechanical description of motion, one needs a high-quality acoustic resonator. This is done using microfabrication, a collection of methods that enables us to create complex structures on microscopic scales. The fabrication of a plano-convex acoustic resonator involves six main steps; photolithography, solvent-reflow, etching, adding spacers, dicing and finally bonding. A diagram of the process up to and including etching is shown in Figure 2.1.

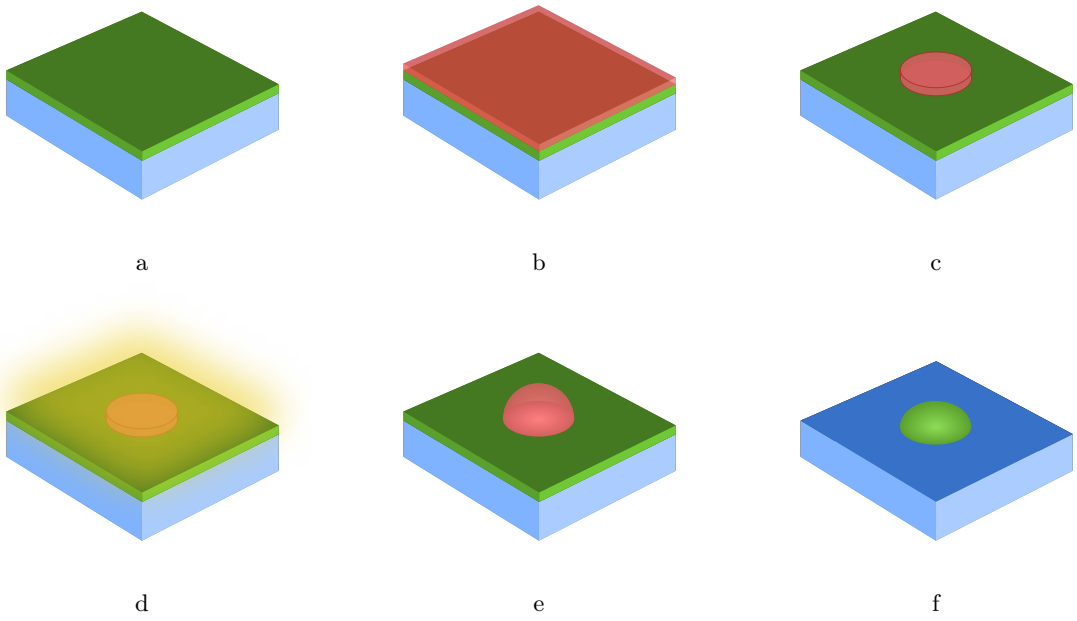

Figure 2.1: Schematic of the HBAR fabrication process. We start out with a crystal (blue) wafer with a piezoelectric (green) thin film (2.1a), on which a photoresist (red) layer is spun (2.1b) and exposed to create cylinders (2.1c). Next, solvent reflow is performed (2.1d) which causes the cylinders to relax into a drop, resembling a spherical cap (2.1e). Finally, the photoresist structure is etched into the piezoelectric thin film (2.1f), resulting in a spherical piezoelectric acoustic mirror.

2.1. Photoresist shaping

2.1.1. Solvent reflow

Solvent reflow is a microfabrication technique that enhances the smoothness of photoresist surfaces by refining and restructuring them [21]. The thermodynamically driven process enables the formation of droplet-like structures by allowing the photoresist fluid to adopt a configuration that minimises the Gibbs free energy [22]. As the photoresist absorbs solvent vapour, its viscosity decreases, enabling better fluidity and reshaping. The reshaped

photoresist resembles spherical caps. Ultimately, the smooth, reshaped photoresist can be etched onto the substrate, creating a high-quality concave acoustic mirror.

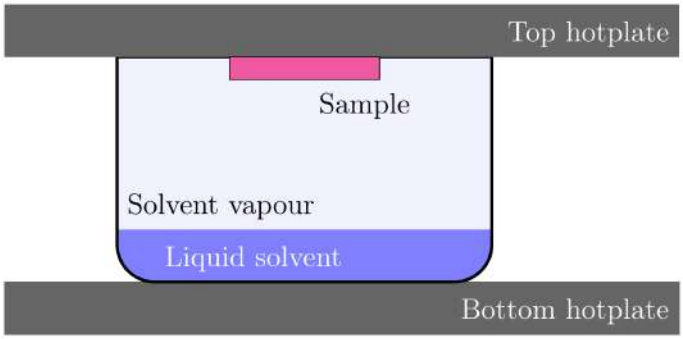

Figure 2.2: Solvent reflow process. Figure from [22].

2.1.2. Greyscale lithography

Greyscale lithography is a fabrication process providing an alternative approach to solvent reflow for creating acoustic mirrors. In this procedure, light intensity is locally modulated during photoresist exposure, facilitating the formation of arbitrary 2.5-dimensional (2.5D) shapes including nonspherical mirrors, in contrast to thermodynamically-driven solvent reflow. An illustration of the technique is presented in Figure 2.3. Applicable to both direct-written lithography (DWL) and masked lithography, comprehensive analyses of these processes are detailed in [22] and [23]. In this study, DWL-based greyscale lithography was employed to fabricate the structures presented in Chapter 5.

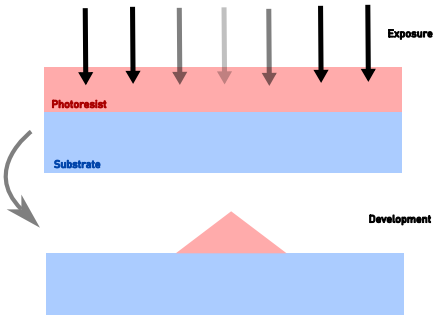

Figure 2.3: **Schematic of greyscale lithography.** Positive photoresist is exposed with varying light doses which allows control of the resulting resist height, thereby enabling writing arbitrary 2.5D shapes. Controlling the dose can either be done with a greyscale mask or by adjusting the intensity of a direct-written laser [22, 23].

2.2. Inductively Coupled Plasma Reactive Ion Etching (ICP RIE)

Inductively coupled plasma (ICP) reactive ion etching (RIE) is a method of dry etching that allows for high etch rates, high selectivity, and low damage processing, making it a suitable method for etching aluminium nitride (AlN). It is a variant of RIE, in which physical ablation is combined with a chemical reaction through the introduction of reactive species [24]. The distinguishing feature of ICP-RIE is the independent control of the plasma density and the ion energy. The technique provides high-quality profile control as the plasma can be maintained at low pressures, in contrast to RIE. A schematic of an ICP RIE etcher is shown in Figure 2.4. The features of ICP RIE etching make it an effective and

flexible method for AlN etching, allowing for precise control over the etching process and outcomes. The devices in this thesis were etched using the OxfordInstruments Plasmalab 100 at the Binnig and Rohrer Nanotechnology Center (BRNC) in Rüschlikon.

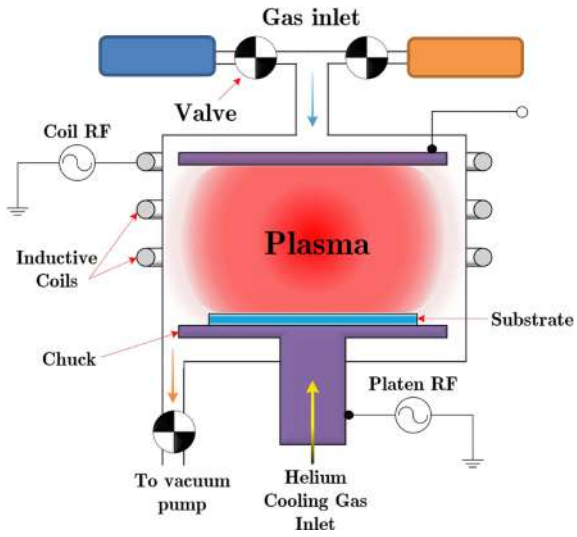

Figure 2.4: Schematic of an ICP RIE machine [25]. The substrate is placed on the chuck into the chamber. The gasses are introduced from the top, controlled by valves that regulate the volumetric rate of each gas. The independent control of the plasma density and ion energy is achieved by a separate voltage between the chuck and the top capacitors (both lavender) and current through the inductive coils that are wound around the chamber. The sample is cooled with a helium gas on the back of the substrate.

A higher ICP power can be employed to boost the etch rate by enhancing the density of the reactive species in the plasma within the chamber.

2.3. Flip-chip bonding

The HBAR chip is bonded to the qubit chip through a flip chip process [1], shown in Figure 2.5. In the first step, four spacers also referred to as pillars, are placed on each HBAR chip. These spacers are made of SU-8 photoresist, an epoxy-based negative photoresist, patterned using masked photolithography. The pillars presented in this work are made with SU-8 2005, with spin parameters depending on the desired heights of the pillars. The second step is applying SU-8 droplet for adhesion to the qubit chip, as shown in Figure 2.5a. This is done using a polydimethylsiloxane (PDMS) stamp, that collects liquid SU-8 from a dummy silicon wafer. The stamp is then pressed onto the qubit chip, exuding some of the SU-8. Lastly, the two chips are aligned and bonded (Figure 2.5b) using the flip-chip bonder FC150 by Smart Equipment Technology. For further details on the bonding process, we refer the reader to [18].

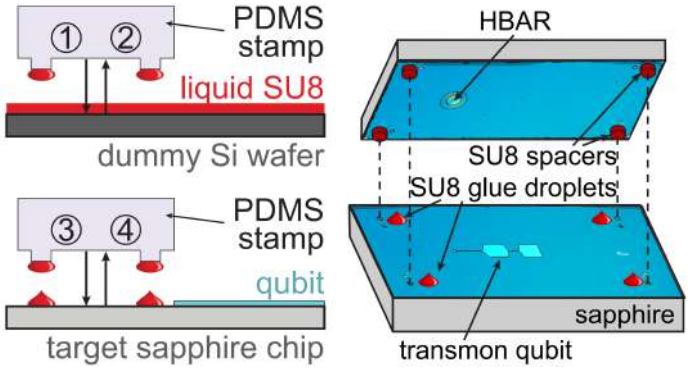

Figure 2.5: **Flip-chip bonding.** After patterning the spacers on the HBAR chip, droplets of liquid SU-8 are collected from a silicon wafer using a polydimethylsiloxane (PDMS) stamp (a, top). These droplets are deposited onto the qubit chip (a, bottom). Next, the two chips are aligned and bonded by baking the resist (b). Figure from [26].

2.4. Cavity installation

After bonding, the $\hbar$BAR device will be placed into a 3D electromagnetic cavity. These cavities are made from a conducting material, typically copper or aluminium, that confines the electric field's eigenmodes within. Aluminium cavities in particular, have high internal quality factors (10^6 to 10^7), minimising losses at cryogenic temperatures [19]. The cavity's frequencies depend on its dimensions and the speed of light.

In this work, the cryogenic measurements have been performed with aluminium cavities, each hosting three $\hbar$BAR devices, as is depicted in Figure 2.6. The larger transmon chip (bottom) rests on the cavity edge, while the smaller HBAR chip (top) is flip-chip bonded to the transmon chip.

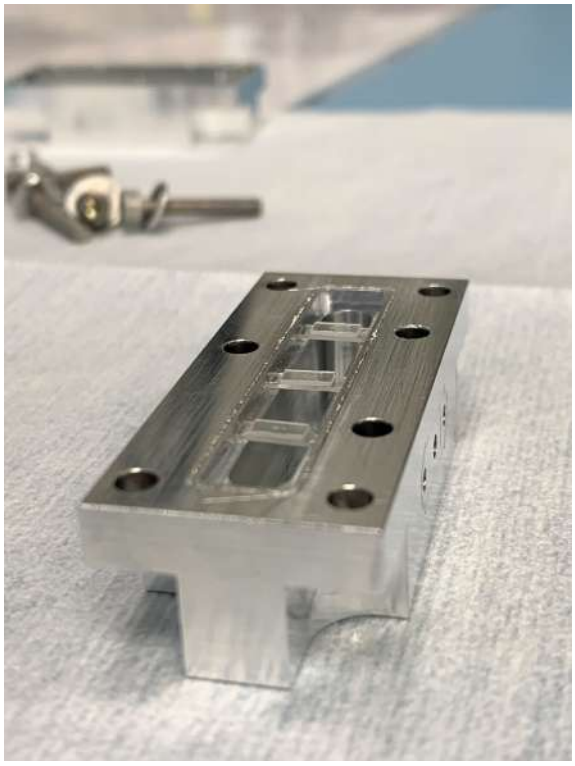

Figure 2.6: Open aluminium cavity containing three $\hbar$BAR devices from the w2274 wafer. The smaller HBAR chip is flip-chip bonded to the longer antennamon chip that rests on the cavity.

HBAR with novel aluminium nitride

Previous works from our group have used HBAR devices based on commercially available aluminium nitride (AlN) on sapphire chips from LumiGNtech [2, 4, 7]. In this chapter, I will present devices that are made with AlN that was grown on double-side polished sapphire by our academic collaborators from the Advanced NEMS Group headed by Professor Guillermo Villanueva at EPFL in Lausanne.

Material properties heavily depend on the microscopic structure, and therefore the growth method. Figure 3.1 showcases how deposition parameters can affect the resulting material.

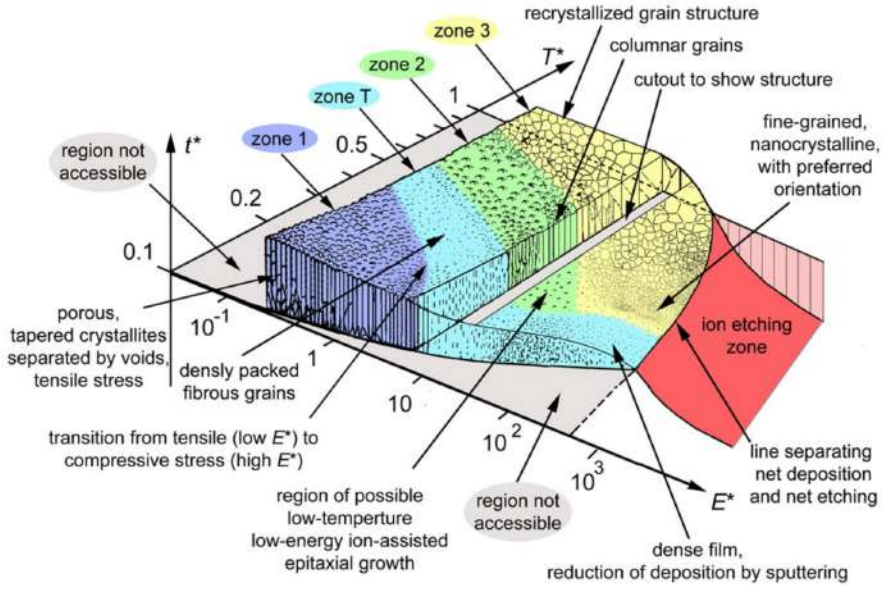

Figure 3.1: Structure zone diagram applicable to energetic deposition; the generalised temperature is represented by T^*, the normalised energy flux by E^*, and t^* represents the net thickness. The boundaries between zones are gradual and for illustration only. The numbers on the axes are for orientation only — the actual values depend on the material and many other conditions and therefore the reader should avoid reading specific values or predictions. Figure and caption adapted from [27].

One of the properties relevant when fabricating acoustic mirrors is how the thin film reacts to a particular dry etch. An important figure of merit for the quality of acoustic mirrors is the root-mean-square (RMS) roughness of the surface. As it turns out, the etch that was used in the fabrication of the device presented in [2, 4] resulted in high (super-nm) RMS roughness for the novel thin film. This is undesirable as this leads to phonon scattering loss at the surface. Therefore, we developed a new etching recipe that results in near- or sub-nm RMS roughness. Section 3.2 covers the development of this etching recipe. Results of cryogenic measurements of the resulting $\hbar$BARs are presented in 3.3.

3.1. Thin film deposition

The thin film was grown on a 420 μm thick double-sided polished sapphire wafer utilising a Pfeiffer SPIDER 600 reactive sputtering cluster. The aluminium nitride was deposited using reactively sputtering in an N_2/Ar atmosphere with 20% Ar while the substrate was kept at 300C. The target was sputtered with a pulsed DC plasma at a power of 1500W. The substrate was biased with a 6W RF generator to minimise reflected power.

3.2. Etching recipes

We experimented with various different etching recipes, focusing on plasmas consisting of BCl_3, Cl_2, and Ar. Results are presented in Table 3.1. Note that the etch rates presented here are averages. Typically, the etch rate varied in time and space. The etch rate is calculated from linear profilometer scans near the apex of the dome, which results in uncertainty of the precise height. The initial etch recipe is identical to the recipe used for the device from [2, 4]. For the chemical compositions of the investigated etches, the following chemical reactions happen [24]. Firstly, the gases are adsorbed onto the AlN surface.

$$Cl^{(gas)} \rightarrow Cl^{(ads)} \tag{3.1}$$

$$BCl_2{}^{(gas)} + BCl^{(gas)} \rightarrow BCl_2{}^{(ads)} + BCl^{(ads)} \tag{3.2}$$

Next, the adsorbed molecules dissociate, generating Cl species at the surface that are highly reactive.

$$BCl_2{}^{(ads)} + BCl^{(ads)} \rightarrow 3Cl^{(ads)} + 2B^{(ads)} \tag{3.3}$$

These Cl species then react with the AlN film, producing $AlCl_3$ and NCl_3

$$6Cl^{(ads)} + AlN \rightarrow AlCl_3{}^{(ads)} + NCl_3{}^{(ads)} \tag{3.4}$$

These products and residues finally desorb from the surface

$$2AlCl_3{}^{(ads)} \rightarrow Al_2Cl_6{}^{(gas)} \tag{3.5}$$

$$3Cl^{(ads)} + B^{(ads)} \rightarrow BCl_3{}^{(gas)} \tag{3.6}$$

The addition of the noble argon gas is relevant for the initial breaking of the III-nitrogen bond of AlN [28]. Note that the adsorbed B originating from the BCl_3 gas is relevant for the desorption of the adsorbed Cl as is evident from (3.6).

Devices from chips W2274c8 and W2274c12 were selected to be bonded to a transmon chip, and subsequently measured at millikelvin temperatures. The microwave measurement results are presented in Section 3.3.

Etch	Chip	Gas rates (sccm) BCl_3:Cl_2:Ar	$P^{RF}_{forward}$ (W)	$P^{ICP}_{forward}$ (W)	$T_{chiller}$ (°C)	r_{resist} (nm/min)	r_{AlN}[i] (nm/min)	$r_{Al_2O_3}$[i] (nm/min)	RMS roughness (nm)	Result
1	W2274c1	40:8:2	120	700	20	121	52	13	10.5	poor, bubbles (see Figure 3.3a)
2	W2274c2	40:8:2	120	700	20	121	52	13	NA	poor, bubbles
3	W2274c3	40:8:2	120	700	20	108	47	11	33.49	poor, bubbles
7	W2274c7	8:24:5	80	500	20	170	92	9	11.66	poor, bubbles
8	W2274c8	40:0:2	120	700	20	49	18	15	1.041	good but very slow
10	W2274c10	40:4:2	120	700	20	83[ii]	34	13	NA	mediocre
11.1	W2274c11	0:0:40	120	700	20	ND	ND	ND	NA	extremely slow, aborted
11.2	W2274c11	40:8:2	188	700	20	193	98	21	NA	meteor stripes
12	W2274c12	40:0:2	120	1000	20	55[iii]	20	18.6	NA	good but slow
14	W2274c14	40:0:2	180	700	20	48[iv]	17	14	NA	fractures in thin film [v]
15	W2275c1	40:0:2	120	2000	20	103	41	38	0.813	good
16	W2275c2	40:0:2	120	2000	20	110	45	42	0.735	good

Table 3.1.: **Etch recipes applied to the novel aluminium nitride** on wafers W2274 (AlN thinfilm on sapphire, white) and W2275 (AlN/Al thinfilm on sapphire, grey). The RMS roughness was determined from a AFM scan of an $30 \times 30\ \mu m^2$ area near the apex of a dome after removing a second order polynomial background, see Appendix A for the data. Not all etches were investigated with the AFM, for these the RMS roughness is labeled as not available (NA). The rates for Etch 11.1 could not be determined (ND) as they were too low. Chips W2274c2 and W2274c1 were etched concurrently. The recipe for W2274c7 was inspired by [24].

To investigate the roughness and quality of the thin film during the fabrication process we used optical and atomic-force microscopy (AFM), in conjunction with profilometry. The surface roughness is measured using a Bruker Dimension Fastscan AFM. Profilometry was performed using a Bruker DektakXT.

Post-etch AFM results for Wafer W2274c8 and our primary device [2] are shown in Figure 3.2, where the top of the dome was inspected. Microscopy is presented in Figure 3.3, and profilometry results are presented in Figure 3.4.

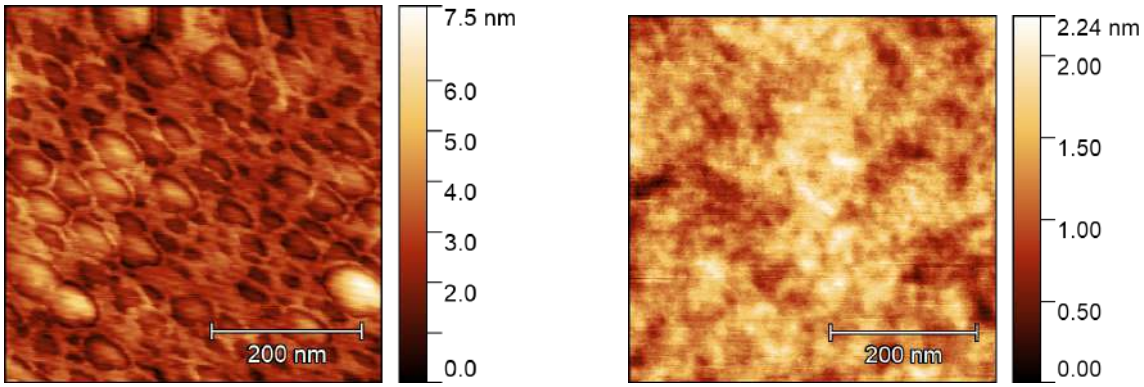

a w2014 b w2274c8

Figure 3.2: **Atomic force microscope (AFM) images of the etched aluminium nitride thin film.** The images are taken on top of the acoustic mirrors of an HBAR on (a) Wafer w2014 with an RMS roughness of 0.85 nm, used for the HBAR device presented in [2, 4], and (b) Chip w2274c8 with an RMS roughness of 0.30 nm, the chip used for some of the devices in this chapter.

[i] These rates could not be measured directly. Instead, they were calculated using the ratio between the radii of curvature, see the W2274 OneNote entry.

[ii] The etch rate over the first 30 minutes was 69 nm/min, and the etch rate over the subsequent 60 minutes was found to be significantly higher at 90 nm/min. Averaged over time, this results in an etch rate of 83 nm/min.

[iii] The etch rate over the first 30 minutes was 45 nm/min, and the etch rate over the subsequent 90 minutes was found to be 58 nm/min. Averaged over time, this results in an etch rate of 55 nm/min.

[iii] The etch rate over the first 30 minutes was 37 nm/min, and the etch rate over the subsequent 130 minutes was found to be 50 nm/min. Averaged over time, this results in an etch rate of 48 nm/min.

[v] The fracturing of the thin film is suspected to be unrelated to the etch recipe. Earlier chips including W2274c4 and W2274c13 also showed signs of fractures after baking the photoresist.

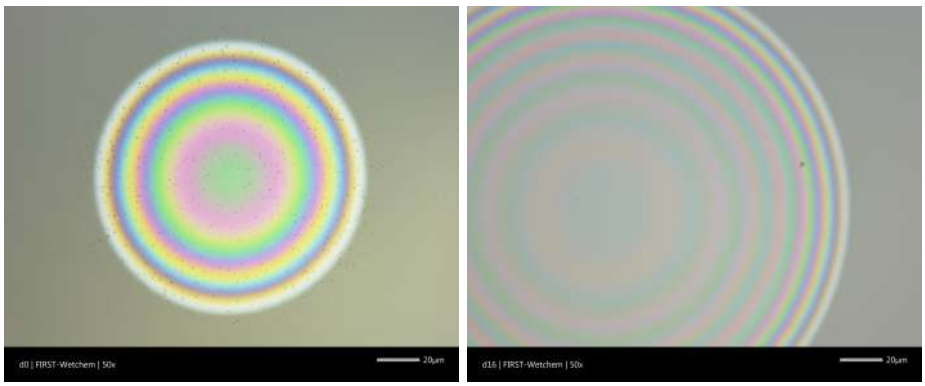

a b

Figure 3.3: Optical microscopy of acoustic mirrors after Etch 1 (a) and Etch 8 (b) from Table 3.1.

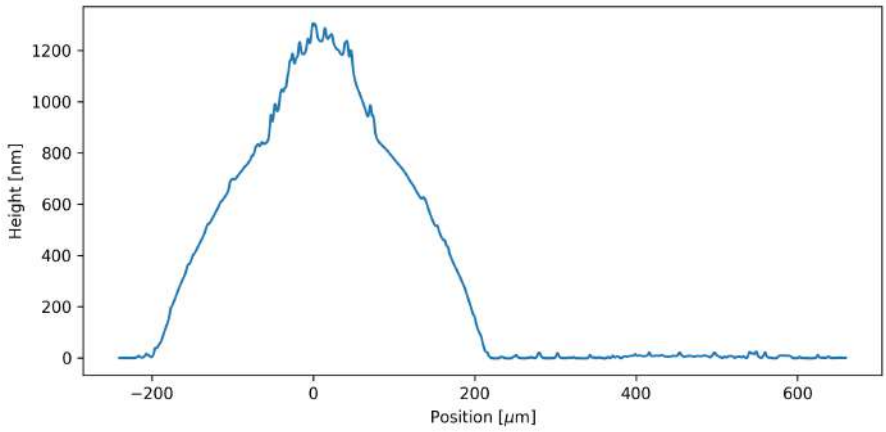

a

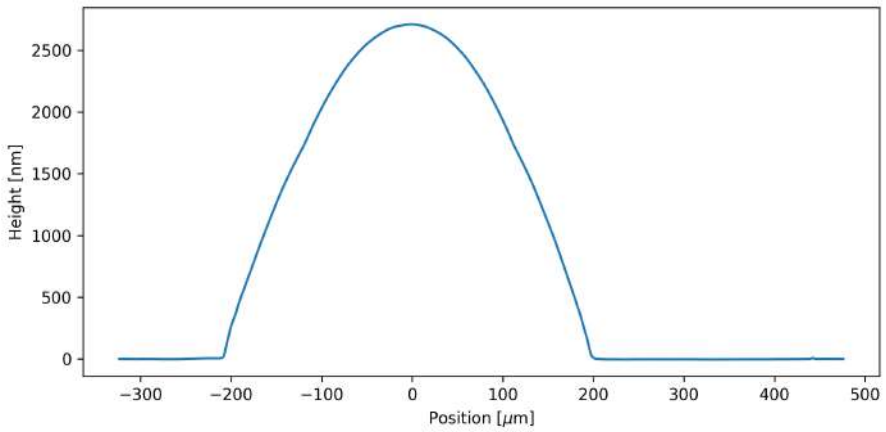

b

Figure 3.4: Profilometry of acoustic mirrors after Etch 1 (a) and Etch 8 (b) from Table 3.1.

3.3. Cryogenic microwave measurement results

Characterisation of six ħBAR devices was done using a cryogenic microwave setup. We are particularly interested in the coherence times T_1 and T_2 of both the transmon and phonon and the coupling rates g_η. For an elaborate overview of the experimental procedures, we refer to [3]. An overview of the results is provided in Table 3.2. The remainder of this section will cover the measurements required to determine these quantities.

Device	Chip	Etch	f_q (GHz)	$T_{1,\eta}^{\max}$ (μs)	$T_{2,\eta}^{\max}$ (μs)	g_η (kHz)	$T_{1,t}$ (μs)	$T_{2,t}$ (μs)	Comments
A	w2274c8	8	4.66	161 ± 10	-	454 ± 5	4.4 ± 0.2	3.1 ± 0.2	-
B	w2274c8	8	5.21	81 ± 5	65 ± 10	539 ± 5	3.1 ± 0.2	5.9 ± 0.2	-
C	w2274c8	8	-	-	-	-	-	-	Qubit not found
D	w2274c12	12	5.26	270 ± 10	530 ± 50	467 ± 1	2.3 ± 0.2	4.4 ± 0.2	-
E	w2274c12	12	-	-	-	-	-	-	Qubit not found
F	w2274c12	12	-	-	-	-	-	-	Qubit not found

Table 3.2.: **Fabricated and measured AlN devices and their parameters.** Here f_q is the transmon *ge*-frequency, $T_{1,\eta}^{\max}$ and $T_{2,\eta}^{\max}$ the maximum single-phonon lifetime and T_2 echo time of the measured acoustic modes, and analogously $T_{1,t}$ and $T_{2,t}$ are the lifetime and T_2 echo time of the transmon qubit. The etch recipes are presented in Table 3.1. Not all quantities were experimentally determined, these are marked with a hyphen (-). No quantum-limited amplifiers were used during the measurements, resulting in significant noise and thus error margins. The error margins presented here are extracted from the covariance matrix of the respective fits.

Figure 3.5 shows a spectroscopy of Device D. Figure 3.6 presents the results of a Rabi experiment, necessary to determine the coupling rate.

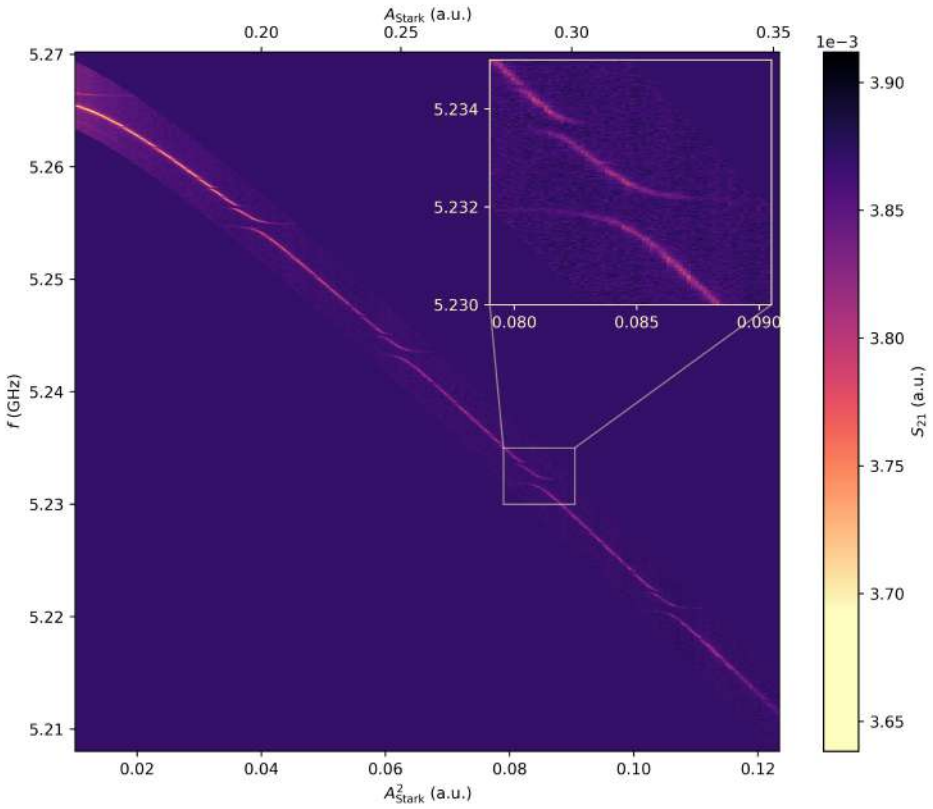

Figure 3.5: **Spectroscopy of qubit spectroscopy of Device D.** The spectrum shows a free spectral range (FSR) of approximately 13 MHz. The dark blue background around the parabolic spectrum is false-coloured.

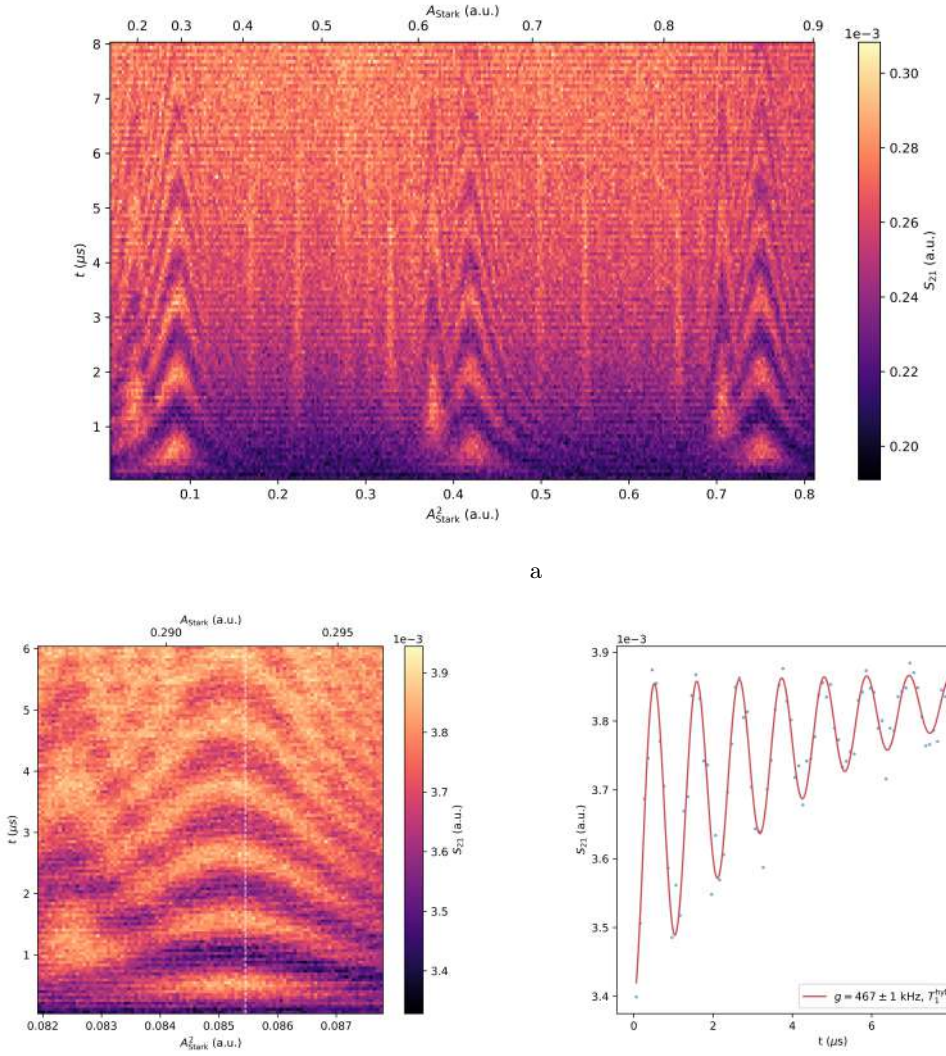

Figure 3.6: **Phonon Rabi measurement of Device D.** The transmon qubit frequencies are tuned by the Stark shift. (a) Phonon Rabi measurement over multiple FSRs. The large features at $A^2_{\mathrm{Stark}} \in \{0.085, 0.42, 0.75\}$ are resonant Rabi oscillations between a fundamental mode and the transmon qubit. (b) Zoomed in measurement around $A^2_{\mathrm{Stark}} = 0.085$, which was used to extract g_η, which sets the oscillation rate as can be seen in (c).

The single-phonon lifetime time T_1 of the phonon modes is measured using a protocol that excites the qubit and then swaps the excitation into the phonon mode. After a variable time t, the mode is read out with the qubit. Results of the longest-lived mode of Device D are presented in Figure 3.7. Figure 3.8 shows the statistics of the lifetimes of Device D and our primary device that was used in [2, 6], showing that Device D had significantly higher T_1 times.

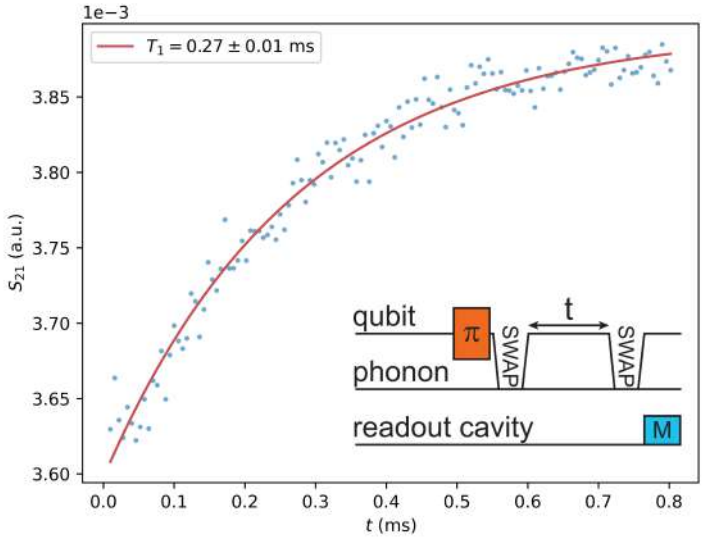

Figure 3.7: T1

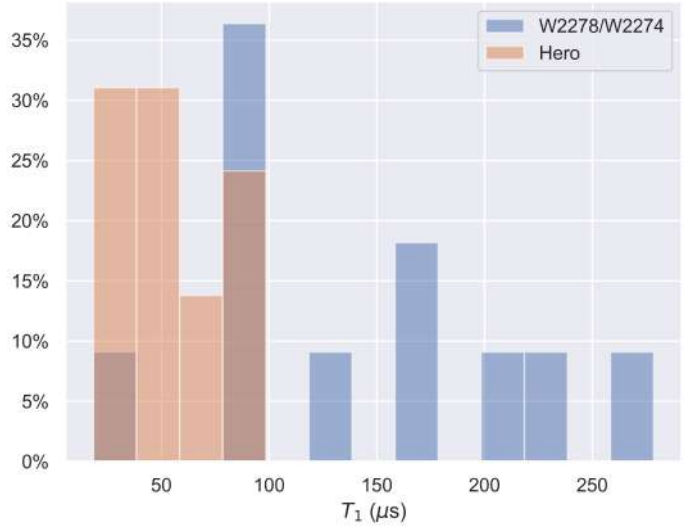

Figure 3.8: Histogram of the T_1 of the measured fundamental modes.

Electrode HBAR

Based on the expression for the HBAR-transmon coupling, various approaches can be considered to enhance its strength. The coupling equation is given by

$$\hbar g_\eta = d_{33} c_{33} \int_D \vec{E}(\vec{r}) \cdot \overleftrightarrow{S}_\eta(\vec{r}) \, dV \tag{4.1}$$

In this section, we present a method to improve both the coupling and selectivity of the HBAR by introducing an electrode between the piezoelectric thin film and the crystal. Through this method, the unidirectionality of the electric field (E-field) can be enhanced. This enhancement occurs as a result of the interaction between the transmon antenna and the electrode, which subsequently influences the E-field inside the piezoelectric material.

As the E-field becomes more unidirectional, the dot product of the E-field vector and the strain tensor corresponding to the bound fundamental mode, $\vec{E}(\vec{r}) \cdot \overleftrightarrow{S}_\eta(\vec{r})$, increases. At the same time, coupling rates to non-longitudinal modes are expected to decrease. Consequently, the electrode leads to a higher coupling rate, effectively enabling us to perform quantum operations between the qubit and phonon mode faster. A higher coupling rate ultimately means that we can perform more operations during the coherence times of the hybrid system. Moreover, the unidirectionality reduces coupling to undesired non-longitudinal phonon modes, reducing losses.

4.1. Electromagnetic simulations with Ansys

The effect of the electrode was quantified using an eigenmode simulation the $\hbar$BAR system in Ansys Electronic Desktop 2021 R2 [29]. The system was analysed with and without the electrode, for a range of gap sizes. The range starts from 0.244 μm, the approximate gap size of the devices in Chapter 3, and ends at 9.244 μm with 1 μm increments. A graphic of the geometry is shown in Figure 4.1.

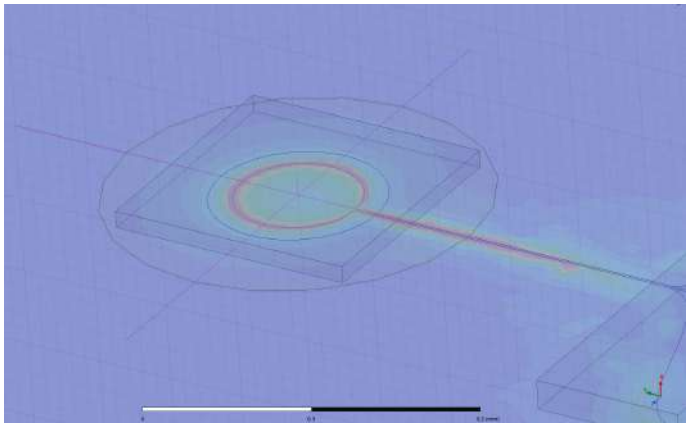

Figure 4.1: **Section of the geometry of the Ansys simulation.** The piezoelectric dome (green) hangs a gap size distance d above the antenna of the transmon (blue). The rectangular boxes are mesh boxes used in the simulation. The electric field along the pink lines were extracted for various gap sizes in the $x-$, $y-$ and z-directions, see the coordinate axis in the lower right corner.

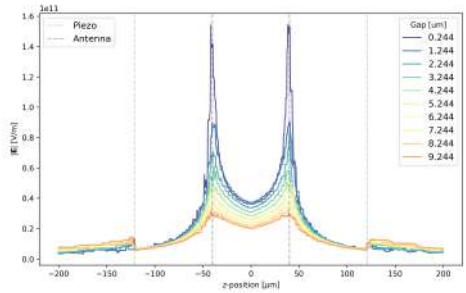

a E_{tot} without electrode

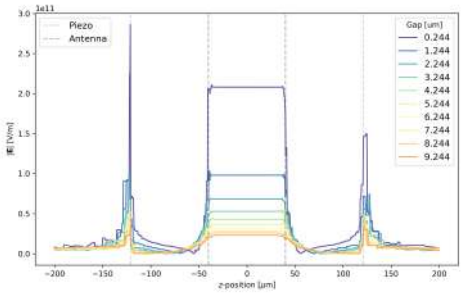

b E_{tot} with electrode

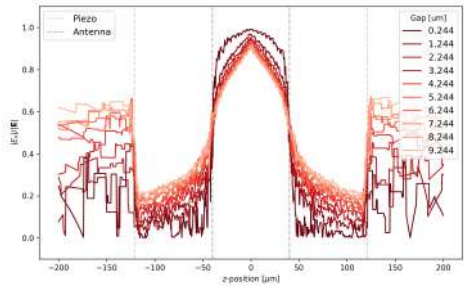

c E_x without electrode

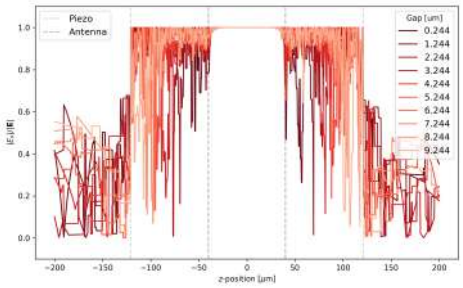

d E_x with electrode

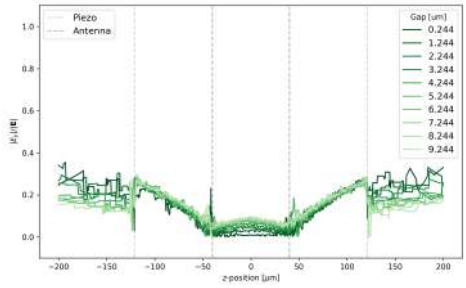

e E_y without electrode

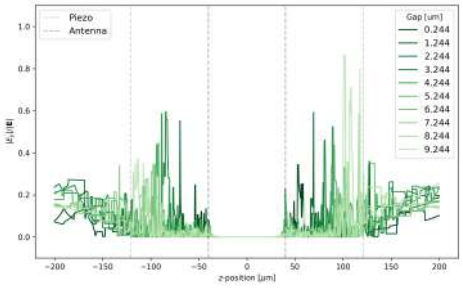

f E_y with electrode

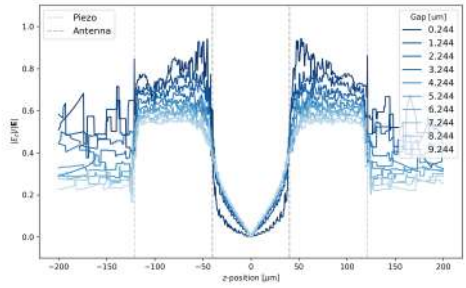

g E_z without electrode

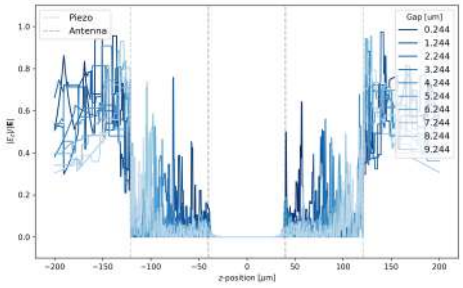

h E_z with electrode

Figure 4.2: **Electric field from the Ansys simulation with and without electrode.** The total electric field (a and b) together with the normalised electric field in the x- (c and d), y- (e and f), and z-directions (g and h) along the z-line for various gap sizes with and without the electrode, respectively, see Figure 4.1. Introducing the electrode increases the portion of the electric field in the longitudinal direction (i.e. x-direction) under the electrode and $E_x/|\vec{E}| \approx 1$ directly above the antenna.

The Ansys simulation results also inform the pillar heights. For the devices presented in this chapter, we aim for an electric field strength in the piezoelectric that is comparable to

the $\hbar$BAR devices presented in the Chapter 3, see Figure 4.3. This adjustment is relevant as the strong capacitive coupling between the electrode and the antennamon causes them to hybridise. Effectively, this means that the electrode will associate with the qubit, creating another loss channel on the HBAR chip. This is undesirable and can partially be negated by weakening the capacitive coupling, which is achieved by increasing the gap size.

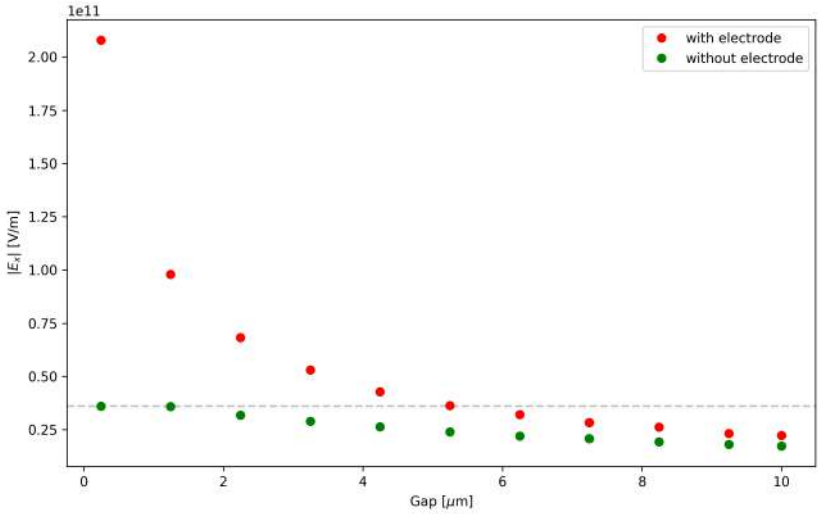

Figure 4.3: E_x strength at the centre of the antenna with and without electrode. The grey dashed line indicates the electric field strength in the simulation of device A from Figure 4.2. At a gap size of approximately 5.5 μm, the HBAR with electrode yields a comparable field strength to this device.

4.2. Fabrication

The fabrication is almost identical to the devices presented in Chapter 3, with a few dissemblances. Most importantly, the deposition of the bilayer metal-piezoelectric thin film involves firstly depositing a 70 nm thick aluminium layer, and then reactively sputtering aluminium nitride as described in 3.1. For etching, a similar recipe as for wafers W2274c8 and W2274c12 (Table 3.1) was employed but with an ICP power of 2000W. The increase in ICP power leads to a higher plasma density and therefore a higher etching rate. After the etch, the devices were cleaned in 130°C DMSO for 30 minutes to clean the front side and remove the adhesive wax from the back side. Figure 4.4 shows the importance of the post-etch solvent clean.

a Pre-DMSO

b Post-DMSO

Figure 4.4: **Post-etch DMSO clean.** Etching the electrode HBAR resulted in a peculiar residue that was not observed when etching the devices presented in Chapter 3. A 30-minute DMSO clean at 130°C removed this residue effectively.

The adjusted etching recipe resulted in similar smoothness but also approximately halved the considerable etching time of roughly 3 hours. The etch rates and roughness are detailed in Table 3.1 and Figure 4.5. Note that the altered etch also affects the etch rates and selectivities. This resulted in domes that are approximately 0.5 μm higher as more of the sapphire is etched when the photoresist is completely removed. Lastly, the height of the pillars (gap size) was increased from 3.25 μm (0.25 μm) to 9 μm (5.5 μm) to account for the increased electric field strength according to the results shown in Figure 4.2.

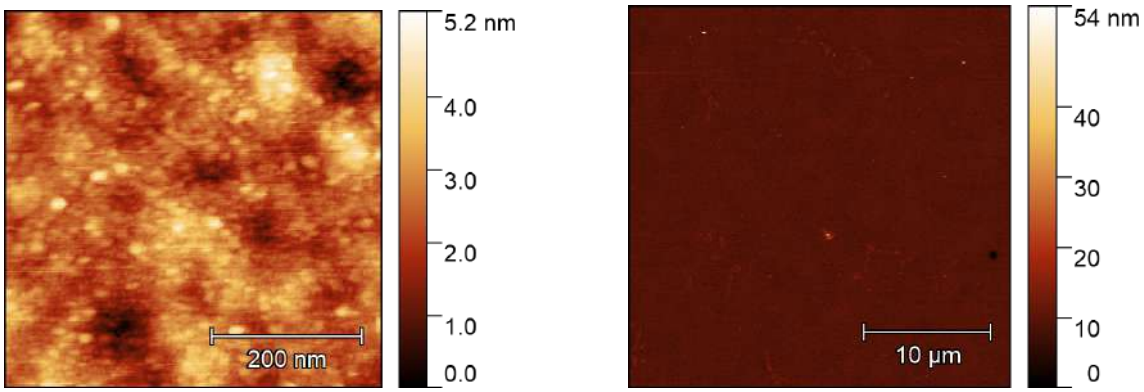

a 500×500 nm^2 patch
RMS roughness 0.64 nm

b 30×30 μm^2 patch
RMS roughness 0.81 nm

Figure 4.5: **Atomic-force microscopy of a dome apex on Chip W2275c1 after etching and cleaning.** The measured RMS roughness is comparable to the 0.43 nm (1.04 nm) RMS roughness for Chip W2274c8 of a 500×500 nm^2 (30×30 μm^2) patch. The difference between W2274c8 and W2275c1 is that the latter has the electrode beneath the AlN thin film and the increased ICP power used in the etch of the latter chip.

Double-sided HBAR

The HBAR device effectively acts as an acoustic Fabry-Pérot cavity, confining phonon modes instead of photon modes. In the preceding chapters, as well as previous works of our group [2, 4], the acoustic resonators were plano-convex. In this simple-to-fabricate geometric arrangement, the piezoelectric dome assumes dual responsibilities: spatial confinement and electromechanical interfacing. These responsibilities, however, require divergent design objectives. A broad, curved architecture is crucial for effective confinement, yet this may inadvertently cause the piezoelectric to couple electric excitations to unintended phononic modes. This section will present an alternative double-sided geometry. In this geometry the two tasks are distributed; a confining dome is etched into the crystal and the piezoelectric is tailored to selectively couple to a single mode.

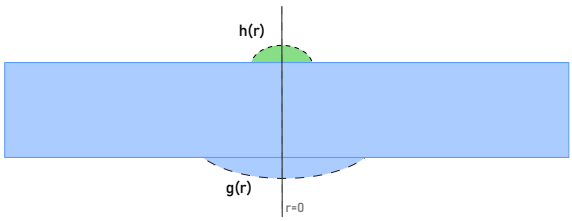

Figure 5.1: **Geometry of the double-sided HBAR.** Acoustic mirrors are etched on both sides of the HBAR chip. The piezoelectric (light green) described by the function $h(\vec{r})$ is shaped to selectively couple to the fundamental mode of the collective structure. On the other side of the piezoelectric, the substrate (light blue) is etched to confine the phononic mode. This structure is described by $g(\vec{r})$ and is referred to as the antipiezo.

5.1. Theory

The acoustic modes of the HBAR is driven by the piezoelectric converting electrical into mechanical energy. The electric field penetrating the piezoelectric causes the material to experience some strain $\overleftrightarrow{S}$. This strain is proportional to the electric field $\vec{E}$,

$$\overleftrightarrow{S} = \overleftrightarrow{d} \cdot \vec{E}. \tag{5.1}$$

The phase of the driving field is given by a model that assumes a constant phase at the piezo-air interface and then propagates that phase according to a plane wave travelling in the z direction to the interface. The amplitude of the generated wave depends on the thickness of the piezoelectric $h(x, y)$ as

$$A(x, y) = \frac{1}{k_z}\Big(1 - \cos(k_z h(x, y))\Big). \tag{5.2}$$

Our objective is to find a piezo shape that will result in a forcing that selectively excites one mode of the acoustic resonator. The driving from the piezoelectric will result in a

displacement u_d at the piezo-bulk interface, which is given by

$$u_d \propto \frac{1}{k_z}\big(1 - \cos(k_z h(\vec{r}))\big)e^{ik_z h(\vec{r})} \tag{5.3}$$

with $\vec{r} \in \mathbb{R}^2$ specifying the x and y position in the plane of the substrate boundary, and $k = 2\pi/\lambda$ is the longitudinal wavelength. Now, we want to drive the fundamental Laguerre-Gaussian mode (LG_{00}) mode

$$u_{00}(\vec{r}) = Ce^{-\frac{|\vec{r}|^2}{2\sigma^2}} \cdot e^{ik_z h(\vec{r})} \tag{5.4}$$

where C is simply a scale factor with units of distance. A shape $h(\vec{r})$ can be derived that ensures that the resulting displacement at the boundary $u_0(\vec{r})$ is Gaussian.

$$u_d(\vec{r}) \propto e^{-\frac{|\vec{r}|^2}{2\sigma^2}} \implies \frac{1}{k_z}\big(1 - \cos(k_z h(\vec{r}))\big) = \tilde{A}e^{-\frac{|\vec{r}|^2}{2\sigma^2}} \tag{5.5}$$

where $\tilde{A} \in \mathbb{R}^+$ is also a scale factor with units of distance. From radial symmetry of the Gaussian function, we can argue that h should be symmetric as well so we will use $r \equiv |\vec{r}| = \sqrt{x^2 + y^2}$ from now on. It follows that

$$h(r) = \frac{1}{k_z}\arccos\left(k_z\big(1 - Ae^{-\frac{r^2}{2\sigma^2}}\big)\right) + \frac{2\pi m}{k_z} \qquad m \in \mathbb{Z} \tag{5.6}$$

where $A \equiv k_z\tilde{A} \in [0, 2]$ is a positive dimensionless scalar that is a measure of the magnitude of the induced displacement by the piezoelectric. In theory, m can assume any integer value. However, from this point forward, we will limit our consideration to $m = 0$ because this minimises the amount of piezoelectric material on the device as this can act as a noise channel (e.g. phonon radiation). We symbolise the function as h_A to underscore its parameterisation. Figure 5.2, shows a crosssection of the parametrised shape together with the first even Taylor coefficients around 0. In Figure 5.3, $h_A(r)$ is plotted for various values of A.

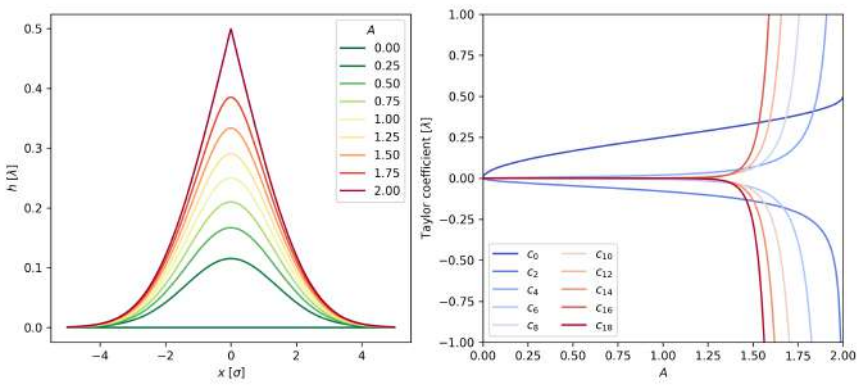

Figure 5.2: Cross-section of the parameterised family of piezoelectric shapes $h_A(x)$ at $y = 0$ (left) and its Taylor coefficients when expanded around $x = 0$ (right).

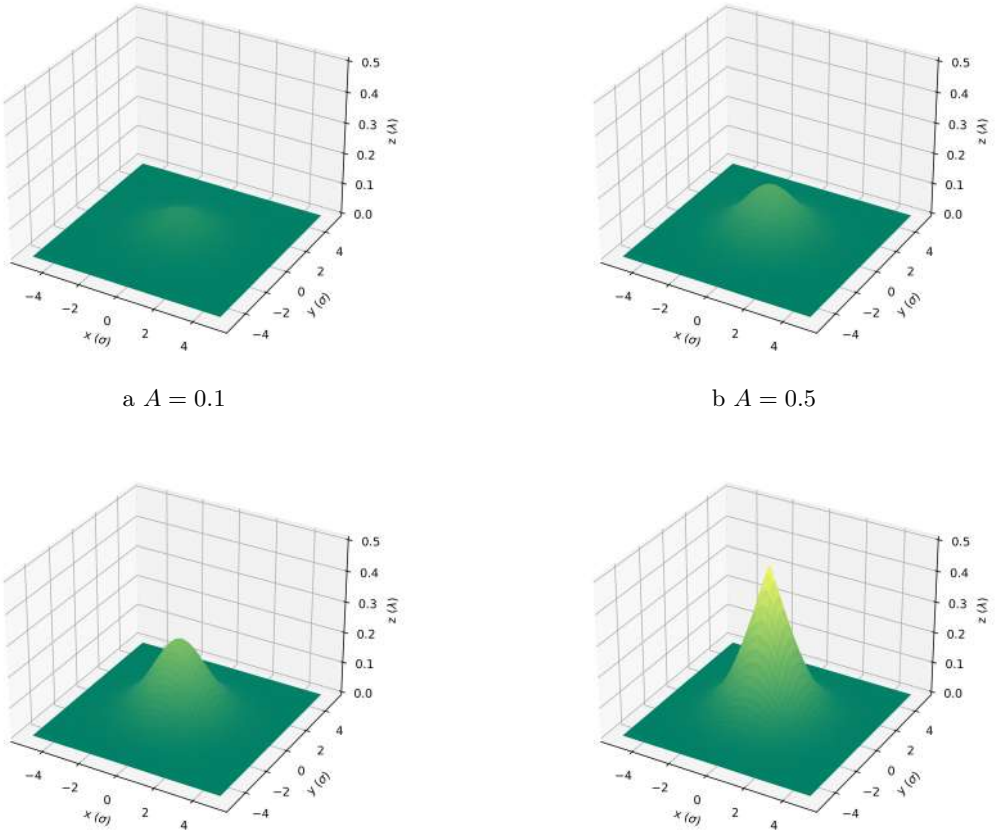

a $A = 0.1$ b $A = 0.5$

c $A = 1$ d $A = 2$

Figure 5.3: Shape of the engineered piezo $h_A(x, y)$ for different values of A.

In the case of sapphire, the longitudinal phonon velocity is $v_l = 1.11 \cdot 10^4$ m/s [3]. The expression for the wavelength λ is

$$\lambda = \frac{v_l}{f} \tag{5.7}$$

where f is the frequency of the acoustic wave. This frequency is equal to the transmon frequency $f_{ge} = \omega_{ge} \approx 6$ GHz. Therefore, $\lambda \approx 2\,\mu$m, and so the piezoelectric structure for $A = 1$ should be approximately half a micron high at the apex.

Now, let us consider what a device exploiting this engineered forcing would look like. Here, it is important to note that the shape of the piezoelectric also changes the acoustic cavity itself. This means that we can not simply design the piezoelectric to couple to the fundamental mode of the plano-convex cavity. To resolve this interdependence, we will investigate two designs, namely

1. a subtracted geometry, or

2. a nonsubtracted geometry.

The subtracted geometry is based on an invariance of the Acoustic Schrödinger equation (ASE) [22, 30]. Specifically, according to the ASE, the acoustic modes of a cavity remain unchanged if one adds a profile to one side, and subtracts the same profile from the right. Starting from a plano-convex HBAR, we add the parameterised piezoelectric function h on the planar side and subtract the same function from the convex dome, possibly with a scale factor k accounting for differences in the acoustic velocities in the different materials. This geometry has the same properties as a plano-convex one, except that the forcing is now engineered to be Gaussian.

The nonsubtracted geometry on the other hand relies on the fact that the function h is approximately domic. The quality of this approach then depends on the parameter A as it influences the curvature of the piezoelectric as well as the anharmonicity of the acoustic cavity, see Figure 5.2. Instead of starting from a plano-convex cavity, one should view this as a convex-convex one.

Schematics of both geometries are shown in Figure 5.4.

a b

Figure 5.4: **Two double-sided HBAR geometries.** (a) The non-subtracted geometry and (b) the subtracted geometry. The subtracted geometry exploits an invariance of the acoustic Schrödinger equation, while the nonsubtracted geometry uses the approximately domic character of h. In both geometries, the piezoelectric is shaped according to the parameterised function h_A, but the opposing antipiezo structures are different. With the non-subtracted geometry, the antipiezo is simply a dome, whereas for the subtracted geometry it is a dome minus h. There are only three parameters for both structures, namely $A \in [0, 2)$, the height of the dome and its radius of curvature.

5.1.1. COMSOL simulations of the forcing at boundary

To confirm the analytical expression for the displacement u_d at the piezo-crystal boundary as a function of the shape $h(x, y)$ of the piezoelectric, we performed 2D frequency-domain simulations using COMSOL multiphysics. The piezoelectric multiphysics package combines solid mechanics and electrostatics. The simulations modelled a cross-section of the upper segment of the HBAR device, namely the piezoelectric and upper 10 μm of the sapphire. The electric field of the qubit was replicated using a parallel plate capacitor on each side of the piezoelectric material, positioned above the vacuum and underneath the substrate, as shown in Figure 5.5. The findings from this simulation are displayed in Figure 5.6.

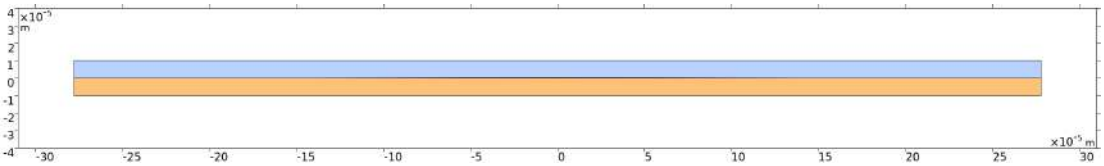

Figure 5.5: Geometry for the 2D COMSOL multiphysics simulation. The system is modelled using three components; vacuum (light blue), a piezoelectric AlN structure (dark orange) described by (5.6) and a sapphire substrate (light orange). Due to the extreme aspect ratio of the simulated geometry (1:20), the thin piezoelectric layer is difficult to see here.

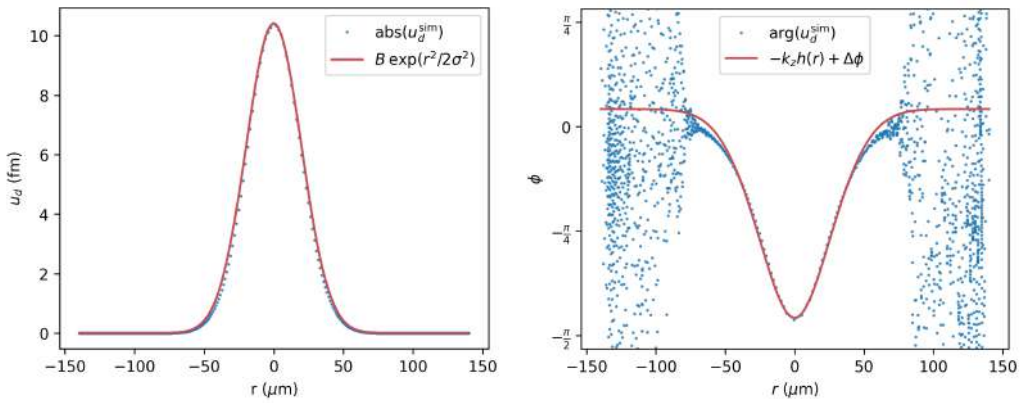

a Magnitude b Phase

Figure 5.6: Data and fit of the magnitude and phase of u_d at the piezo-crytal boundary of the COMSOL simulation. Note that there are only two fit parameters, B and $\Delta\phi$ which are taken such that the data point at $r = 0$ coincides with the fit.

5.1.2. Beam propagation simulations for forcing overlap and linewidth

Now that we established an approximate analytical expression for the displacement at the piezo-crystal boundary, we can employ acoustic beam propagation simulations [21] to characterise the modes and selectivity of the subtracted and non-subtracted double-sided HBARs. In particular, we employ `BeamProp`[i] [22], a software package based on [21] maintained by our group. We focus on the case $A = 1$, future work should explore the rest of the parameter space.

To characterise the overlap between a particular forcing profile and a mode profile, we introduce the forcing overlap O_η of a mode η as a figure of merit

$$O_\eta = \frac{|\langle F|u_\eta\rangle|}{\sqrt{\langle F|F\rangle \cdot \langle u_\eta|u_\eta\rangle}} \in [0,1] \tag{5.8}$$

where F is the forcing, and u_η is the profile of mode η, at the piezo-substrate interface. In the beam propagation simulations, we model the forcing by propagating as an initial displacement u_0. This displacement is propagated for n roundtrips at different frequencies f. After doing so, we identify the supported modes of an acoustic cavity by looking at the frequencies with the highest intensity.

[i] https://gitlab.ethz.ch/hyqu/beamprop_modules

We now determine the forcing overlap as a function of front-back misalignment to investigate the susceptibility of fabrication imperfections. We use the parameters $A = 1$, dome height $H = 1\ \mu$m and radius of curvature $R = 6.44$ mm[ii]. The width of the piezoelectric structure σ then depends on the geometry; nonsubtracted (ns) or subtracted (s). For this set of parameters, we found that $\sigma_{\mathrm{ns}} = 21.32\ \mu$m and $\sigma_{\mathrm{s}} = 13.93\ \mu$m yield (fundamental) Gaussian modes[iii] with the same beam width. Results of these simulations are presented in Figure 5.7.

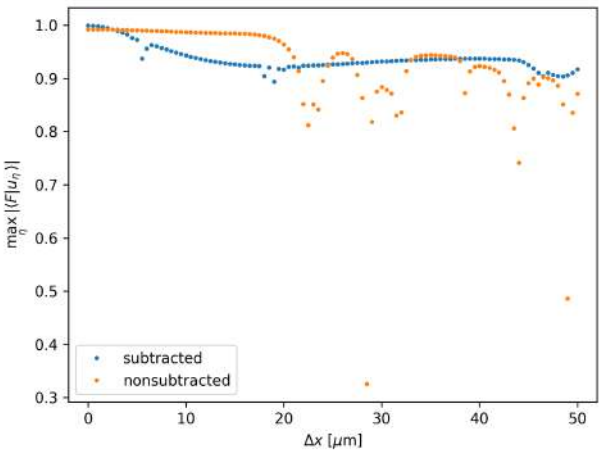

Figure 5.7: **Maximum overlap as a function of misalignment for the subtracted and non-subtracted geometries.** Both geometries yield forcing maximum overlaps $\max_\eta O_\eta > 0.9$ for misalignment within 10 μm. The subtracted geometry can reach a unit forcing overlap at perfect alignment, but it is more sensitive to misalignment compared to its nonsubtracted counterpart.

The forcing overlap only partially characterises the piezoelectrically driven HBAR. Another important figure is the linewidth of the acoustic mode. The linewidth characterises the loss rate, and can also be estimated using `BeamProp` simulations. This is done by propagating the displacement field until it converges, meaning the losses cancel out the gained intensity by performing more roundtrips. These losses can be due to geometry, internal losses κ or reflection losses at the boundary. In Figure 5.8, we present results of two double-sided HBARs with perfect alignment. We only model geometric losses to provide an upper bound for the expected linewidth. As can be seen, the linewidth of the nonsubtracted design for this parameter set is an order of magnitude bigger.

[ii] The dome parameters (i.e. height and radius of curvature) were informed by the geometries of the HBARs presented in Chapter 3.

[iii] Since the cavities are not perfectly spherical, it is inaccurate to talk about the fundamental Gaussian mode. In this context, we mean the mode that is *approximately* Gaussian.

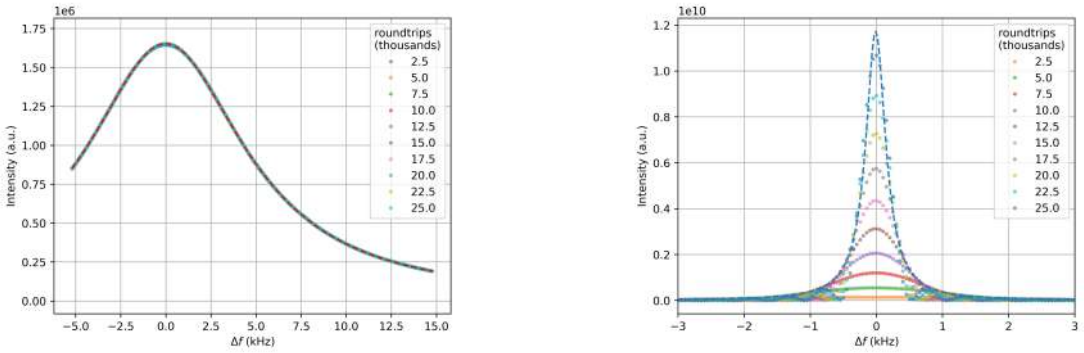

a b

Figure 5.8: **Simulated frequency spectra of the (a) non-subtracted and (b) subtracted double-sided HBAR geometries with A = 1.** The frequency $\mathbf{f = f_0 + \Delta f}$ is plotted relative to the corresponding resonance frequency f_0 that differs between the two geometries ($f_{0,\mathrm{ns}} = 5.987$ GHz and $f_{0,\mathrm{s}} = 5.992$ GHz). Modelling only geometric losses, the linewidths $\Delta\nu$ of the fitted Lorentzians are 10.70 and 0.37 kHz, respectively. No internal or reflection losses were modelled. The intensity profile of the non-subtracted geometry already converged after 2500 roundtrips, whereas the profile for the subtracted geometry had not converged after 25000 roundtrips, therefore the 0.37 kHz is only a lower bound for the linewidth. These results indicate that the non-subtracted geometry is severely limited by geometric losses for the parameter set $A = 1$, $H = 1\ \mu$m and $D = 6.44$ mm.

5.2. Fabrication

The double-sided ħBAR fabrication is significantly more complicated than the plano-convex version, as it requires producing nonspherical photoresist structures and precisely aligning these on either side of the crystal to each other. There exist two techniques presently outside the domain of expertise of our laboratory to do this, namely backside alignment and greyscale lithography. In the following two sections, we will present foundational work and results towards fabricating these devices. In section 5.2.3, we propose a concrete fabrication workflow.

5.2.1. Greyscale lithography process

We employed direct-written laser greyscale lithography to produce the prototypical photoresist structures for the double-sided dome. For the most part, we followed [22], but made notable changes in the resist and exposure recipes. In particular, we brought the resist thickness from 9 μm down to 5 μm, for two reasons. Firstly, the piezoelectric structures of the double-sided HBAR are targeted to be around 0.5 μm high at the apex (see Section 5.1), assuming a sapphire wafer with an aluminium nitride thin film and $A \approx 1$. The desired height of the photoresist structures depends on the etch selectivity between AlN and the photoresist. For Etch 8 and Etch 12 used for the devices in Chapter 3, the etch selectivity $r_{\mathrm{resist}}/r_{\mathrm{AlN}} \approx 2.7$ (see Table 3.1) and so we require photoresist structures of approximately 1.4 μm. Reducing the resist height is therefore possible, and improves the z-resolution as there are more valuable grey tones. Secondly, we noticed the formation of bubbles during development. In the case of positive resist, this might indicate that the light intensity during exposure was too high [31] and reducing the thickness of the photoresist layer allows for a decreased exposure intensity. Indeed, when we reduced the resist thickness and employed lower exposure intensities we did not find the same formation of bubbles after development.

Moreover, a higher n-over mode is used to reduce stitching effects [23, 32], as is illustrated in Figure 5.9. For the exposures presented in this work, we use n-over 20, as this is the

highest mode available on the DWL66+ laser lithography tool at the FIRST cleanroom. This tool features the Standard Grayscale Mode, supporting 128 grey levels and n-over modes 1 (i.e. no stitching reduction), 2, 4, 10, and 20. Previous studies have proposed the utilisation of n-over 4 to balance stitching reduction with exposure time [23]. Nevertheless, we argue that the advantages of minimising stitching artefacts are more significant than the drawback of extended exposure time.

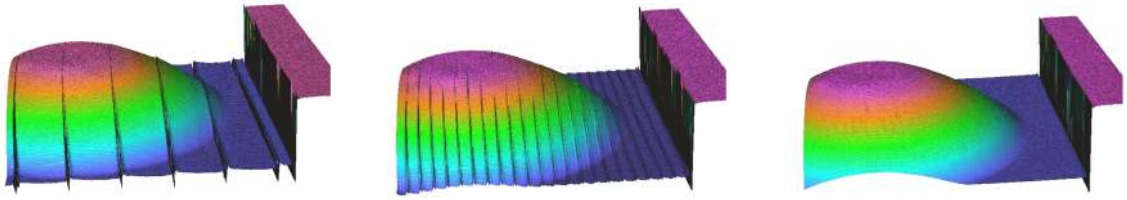

a No stitching reduction b n-over-4 c n-over-40

Figure 5.9: **Illustration of stitching effect reduction using n-over mode.** Figures adapted from [32].

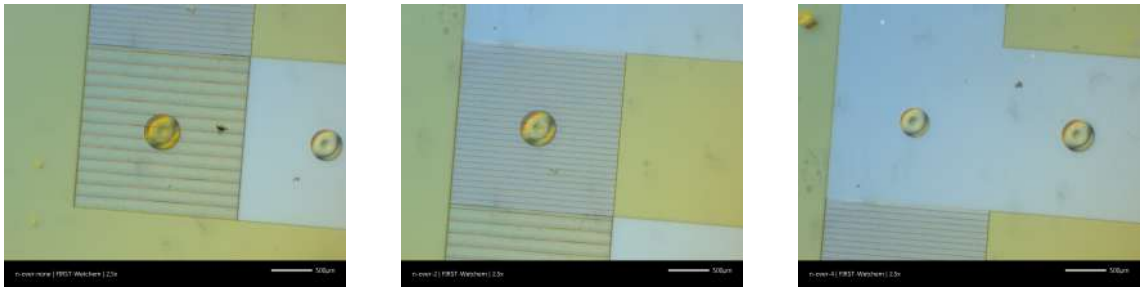

a No stitching reduction b n-over-2 c n-over-4

Figure 5.10: **Employing n-over modes for stitching reduction.** Microscopy of developed 9 μm thick AZP4620 photoresist after a greyscale DWL exposure with various n-over modes with the same intensity, filter and laser power. Note that the dose is not adjusted across n-over modes, so effectively it is multiplied. In the patch with $n = 4$, the photoresist was developed up to the sapphire substrate. Notice that there are bubble formations in the regions where the photoresist is developed, which might indicate that the intensity was too high during exposure.

We employ the software package dome-tookit presented in [22] to generate the `bmp` files. Several improvements have been made in this work, and the package now includes easy-to-use Jupyter notebooks [33] for calibration and generation of the `bmp` files. The calibration procedure can directly use profilometer data stored in `OPDx` or `csv` files through the integration of the opdx-analysis package, created for this work to facilitate profilometry data analysis.

The fabrication workflow for greyscale DWL is as follows. Firstly, one has to prepare a `bmp` file[iv] that can be converted into a `job` file using the software provided by Heidelberg Instruments on the DWL PC in the FIRST cleanroom. During the conversion, the pixel size, n-over mode, stripe width and greytable is selected. The greytable maps grey values of the `bmp` file to values that will be used by the DWL machine. Since the DWL at FIRST supports 128 values, one can either prepare a `bmp` file with 128 grey values or one with 256 grey values and apply the `gr128-255` greytable. In the cleanroom, the sample is cleaned and prepared with a photoresist. Cleaning is done by sonicating the sample in acetone and consequently in isopropyl alcohol (IPA) at maximum power for 3 minutes and 1 minute, respectively. After blow drying the sample with N_2, and baking it at 120°C for 2 minutes,

[iv] See this example notebook for an elaborate example of how to generate and use a dose test to make a `bmp` file.

the photoresist is spun. In this work, we found that AZ4562 [34] resist spun at 6000 rpm yielded a reliable and uniform photoresist layer of around 5 μm. However, depending on the height of the desired structures one could consider choosing a different spinning recipe. Note that uniformity of the coating is essential for greyscale lithography as irregularities in the coating can gravely affect the developed photoresist structure. After preparing the resist layer, the sample can be exposed. For further information on photoresist spinning for greyscale lithography we refer to [23].

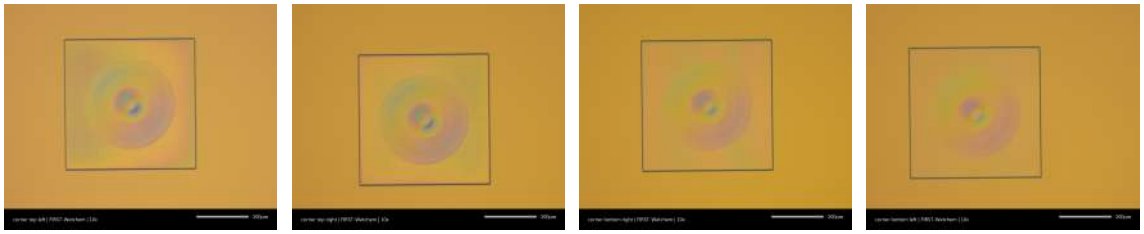

a top left b top right c bottom right d bottom left

Figure 5.11: **Microscopy of four exposed dies after development.** The exposure was done with n-over-20 mode on a 5 μm thick AZ4562 photoresist. The results indicate that the photoresist structures are consistent across dies during one exposure.

During this work, we also explored the use of AZP4620 for greyscale lithography, the photoresist we use for solvent-reflown domes. Nominally, AZP4620 and AZ4562 are identical. However, when using the 5500 rpm photoresist recipe for the domes and using this for greyscale lithography we encountered issues with the resist uniformity, see Figure 5.12. Tests with AZ4562 at 6000 rpm yielded reliable uniform photoresist layers, see Figure 5.11.

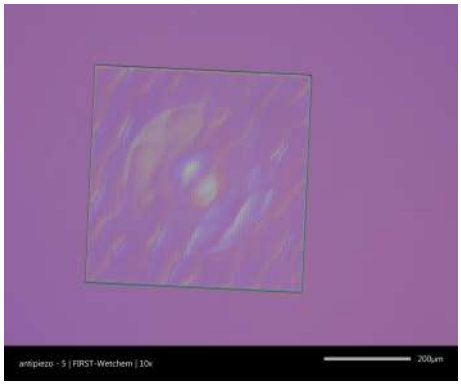

Figure 5.12: **Effects of photoresist nonuniformity on greyscale lithography**. Microscopy of a n-over 20 greyscale exposure using photoresist AZP4620 spun at 5500 RPM for 90s with a spinup of 3s. This is the same photoresist recipe that we use to define the cylinders for the solvent-reflown acoustic mirrors. The wavelike pattern stretches outward from the wafer centre, indicating that the issue lies with the spinning of the photoresist.

5.2.2. Backside alignment

The double-sided geometry requires front-to-back alignment, which was not required for earlier ħBAR devices. Several options are available for this technique

1. topside alignment through transparent wafer, see Figure 5.13a
2. backside alignment through transparent wafer, see Figure 5.13b
3. backside alignment with overlay
4. backside alignment with crosshair

Options 3 and 4 employ the backside cameras like in Figure 5.13b. However, unlike transparent backside alignment, these techniques capture an image of (overlay) or position on (crosshair) the mask when the sample is not loaded. After capturing the image or the position of the crosshair, it is used to align the sample. The overlay and crosshair methods can also be employed for nontransparent materials. In practice, options 2-4 are limited to chips with a minimum width of 2 inches because of constrained movement of the two backside optics. For the devices fabricated in Chapters 3 and 4, 1-inch square chips were utilised to conserve material. Consequently, transparent topside alignment is preferred if it offers adequate alignment precision. Experimental results confirm that transparent topside alignment can achieve accuracy within 5 μm, verified using through-wafer microscopy after applying the technique to a sapphire sample. Cleanroom staff discussions indicate that options 3 and 4 can yield an alignment precision of $2 \sim 3$ μm, assuming that the backside optic is well-aligned.

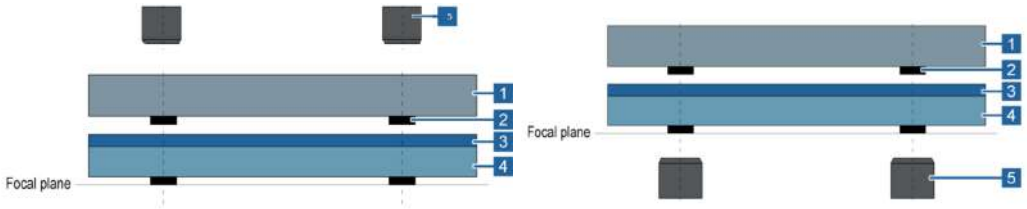

a Topside alignment b Backside alignment

Figure 5.13: Top- and backside alignment. The marked items are the (1) mask, (2) mask and wafer alignment patterns, (3) photoresist, (4) wafer and (5) the alignment optics. [35]

5.2.3. Proposed fabrication procedure

Combining the knowledge from sections 5.1.2, 5.2.2 and 5.2.1, we now present a proposal for the fabrication procedure of a double-sided ħBAR device in Table 5.1.

Step	Crystal (Sapphire)	Piezo (AlN)
1.1		Frontside global alignment marks (GAMs)
1.2	Backside GAMs front-back aligned to frontside GAMs	
2	Greyscale photolithography of acoustic mirrors aligned to backside GAMs	
3	Etch	
4	Chip alignment marks (CAMs)	
5		Piezoelectric structures aligned to GAMs
6		Etch
7		Pillars

Table 5.1.: **Proposed fabrication procedure for the double-sided HBAR.** After steps 2 and 5 a smoothening of the photoresist structures with reflow could be considered [22].

There are several considerations relevant to the fabrication of the double-sided HBAR that do not emerge for HBARs with a plano-convex geometry. In particular, it is essential to protect structures on one side while processing the other side. One proposal is to cover the thin film with e-beam or photoresist that protects it when performing fabrication of the crystal side. Notably, it has been shown that the AZ400k developer affects the roughness of the AlN thin film, as it can act as a wet etchant [24]. The thin film roughness is especially prone when it is single-crystal, i.e. when epitaxially grown, as it can result in anisotropic wet etching in the c-axis direction [36]. Moreover, the adhesive wax necessary for thermal conductivity to the chuck of the ICP-RIE etcher could also have adverse effects on the backside structures. Preliminary tests on unprocessed AlN thin films have indicated that this can be negated by cleaning the sample in warm acetone combined with light scrubbing with a cleanroom wipe, followed by sonication in IPA. Other more aggressive solvents such as dimethylsulfoxide (DMSO) at 130°C could also be considered to remove the adhesive.

There are also alternative approaches one could take to fabricate the proposed piezo and antipiezo structures, including masked greyscale lithography and solvent reflow. Within the option of greyscale direct-written laser lithography, it is still to be investigated how to optimally reduce the stitching effects. Possibilities include solvent reflow, thermal reflow, or employing a different n-over or CI-over modes[v] [32].

Taking into account the limitations of the DWL, it becomes apparent that its application for large-scale areas can be time-consuming [23]. The situation becomes even more demanding when utilising the n-over mode, which increases the exposure duration proportional to the number of passes. For instance, a single-pass exposure of a $50 \times 50\text{mm}^2$ area necessitates approximately 70 minutes [32], thus an equivalent area would require a full day of exposure under the n-over-20 mode. This substantiates that employing the DWL does not scale efficiently for larger chips. A feasible solution to this problem is a two-step exposure approach. The sections necessitating intricate greyscale patterning could be addressed using DWL in the n-over-20 mode while the remaining areas could be exposed using a faster binary mask or direct-written laser lithography step.

[v] Note that the DWL66+ at the FIRST cleanroom is currently equiped with the Standard Grayscale Mode, supporting n-over modes 1, 2, 4, 10, and 20. To utilise the n-over mode 40 or CI-over modes, the system would need to be upgraded with the Professional Grayscale Package from Heidelberg Instruments.

Chapter 6

Conclusion

We presented progress on the fabrication and design of high-acoustic bulk acoustic resonators (HBARs) for circuit quantum acoustodynamics. Three designs were considered; a plano-convex device made with a novel aluminum nitride thin film with and without an electrode between the piezoelectric and the crystal, and a double-sided HBAR engineered for optimal coupling selectivity.

A new etching recipe was developed for the novel aluminium nitride to reduce the root-mean-square roughness of the etched AlN below 1 nm. Six of the fabricated HBARs have been flip-chip bonded and cryogenically measured. Two of these have support phonon modes with T_1 lifetimes exceeding 100 μs. One device has been shown to support an acoustic mode with $T_1 = 270 \pm 1$ μs and a quality factor of $Q = f \cdot T_1 \approx 1.4 \cdot 10^6$, competitive with state-of-the-art electromechanically coupled acoustic resonators in the GHz regime [37].

Simulations have been performed for the electrode HBAR indicating that the electric field unidirectionality significantly improves when introducing an electrode between the piezoelectric and crystal. Electrode HBAR devices with a 40 nm thick aluminium electrode have been fabricated up to flip-chip bonding using the same aluminium nitride thin film as the aforementioned device in conjunction with a similar etch recipe.

Lastly, concrete steps towards the double-sided HBAR have been taken. An approximate analytical description of the forcing at the piezo-crystal boundary is presented, which was used to derive a family of piezoelectric shapes that exhibits optimal coupling selectivity to a Gaussian fundamental mode. The shapes are parameterised by the wavelength λ, the beamwidth σ and a dimensionless parameter $A \in [0, 2)$. Two double-sided HBAR geometries have been considered based on these piezoelectric shapes, namely the subtracted and nonsubtracted variants. Using simulation software based on [21] we established a relationship between the overlap of the forcing function and the mode, and the misalignment between the two opposing structures to gauge the robustness against fabrication imperfections. Furthermore, an estimate of the linewidth for the two geometries is presented for the case $A = 1$, which indicates that the nonsubtracted variant suffers from increased geometric loss compared to its subtracted counterpart.

Chapter 7

Outlook

The extended coherence times of the phononic modes in the presented device pave the way for new experimental opportunities. Potential applications include protocols where the energy primarily resides in the phononic mode, such as the beamsplitter protocol described in a recent preprint [7]. In conjunction with the enhanced coupling rate, this device may also prove advantageous for demonstrating a mechanical qubit. When the transmon qubit approaches resonance with a phononic mode, the two hybridise, and the resulting hybridised system inherits the transmon's anharmonicity, enabling operation as a qubit system.

Regrettably, the transmon coherence times of the measured $\hbar$BAR devices were significantly shorter than those reported in previous studies [2, 4, 7], which limits their overall applicability. Nonetheless, given the relatively high fabrication yield (2 out of 6 measured $\hbar$BAR devices exhibited acoustic modes with $T_1 > 100\ \mu$s), the reproducibility of these HBAR devices is anticipated.

Regarding the double-sided HBAR, significant steps still need to be taken in both simulation and fabrication. First and foremost, the smoothness of the photoresist pattern is not yet sufficient. There are two evident solutions, namely applying a short reflow step as was considered in [22] or upgrading the direct laser writer with the Professional Grayscale Lithography package. Alternatively, one could consider writing the small piezo structures within one stripe of the direct laser writer [32], or experimentally optimise the stitching by applying a corrective filter in software when generating a bitmap file. Another option would be to explore the applicability of solvent reflow to create the parameterised shape approximately.

Furthermore, a considerable portion of the parameter space remains unexplored. Due to time constraints, this work focused on $A = 1$ and an antipiezo with a fixed radius of curvature. It is possible that the non-subtracted design outperforms the subtracted geometry in certain aspects, such as resilience to misalignment. Additionally, an investigation of linewidth versus misalignment is necessary for both geometries and a range of A values to provide a better understanding of the fabrication possibilities.

The techniques developed for the double-sided HBAR can be employed in other applications. For instance, a phononic shield around the acoustic mirror could be incorporated to protect against surface acoustic waves within the same photolithography and etching steps as the acoustic mirror. Moreover, grayscale lithography can be utilised to fabricate domes with large radii of curvature, which are useful in transduction experiments where the goal is to match the acoustic beam waist to the optical beam waist to optimise overlap.

The primary unresolved inquiry from this study concerns the remarkable coherence times observed for the phononic modes in the device fabricated using the novel AlN material. This phenomenon could be attributed to the novel material itself, the employed etching technique, or the geometry featuring a smaller radius of curvature. To address this question, one could simply apply the same etching process to an AlN-on-sapphire wafer obtained from LumiGNtech. Additionally, investigating the correlation between coherence time and temperature may provide insights into the underlying loss mechanisms. Specif-

ically, two-level system (TLS) defects exhibit a distinct temperature-dependent influence on coherence times. If losses predominantly arise from TLS defects, the quality factor Q would exhibit an increase as a function of temperature.

Acknowledgments

First of all, I would like to thank Yiwen and everyone from the Hybrid Quantum Systems Group. The friendly and supportive culture in the group together with the drive for excellent research made the perfect environment to conduct my master's thesis. Moreover, I wish to thank my predecessors Pedro Rosso Gómez and Thomas Palmen for their work in greyscale lithography. I count myself lucky to have had the chance to work with you all.

I would like to acknowledge Yiwen for proposing the subtracted double-sided HBAR geometry and Hugo for his hand in deriving the forcing function.

I would also like to extend my thanks to the cleanroom staff and fellow users. Their helpfulness has been paramount for my work. I am especially thankful to Ute Drechsler from BRNC, whose expertise in plasma etching and backside lithography was fundamental in this work. I also wish to acknowledge the regulars at FIRST cleanroom outside the group, namely, Alex Flasby, Dante Colao, Giorgio Bonomo, Filippo Ciabattini, Felix Helmrich for always offering me a hand or advice when needed.

I would like to express my gratitude to Marco Liffredo and Prof. Villanueva from the Advanced Nano-electromechanical Systems Laboratory at EPFL in Lausanne. Their generosity in providing us with the AlN and AlN/Al on sapphire wafers was crucial for this research.

Furthermore, I would like to express my appreciation to Tony Mate, for providing me with the much-needed boosts during challenging times. Your support has been pivotal in propelling my progress.

A special acknowledgement goes to ChatGPT. Your assistance in coding, rephrasing sentences, or crafting LaTeX tables has truly accelerated my work, making the process more efficient and enjoyable.

And finally, to my supervisor, Max, I extend my deepest gratitude. Our various cleanroom, simulation, and snow parties have been an immense joy. Your kind guidance and support throughout this project have been invaluable and helped me realise how beautiful and exciting experimental physics is.

I am grateful to have worked alongside such a remarkable group of individuals. My deepest thanks to all of you ♡

Atomic force microscopy

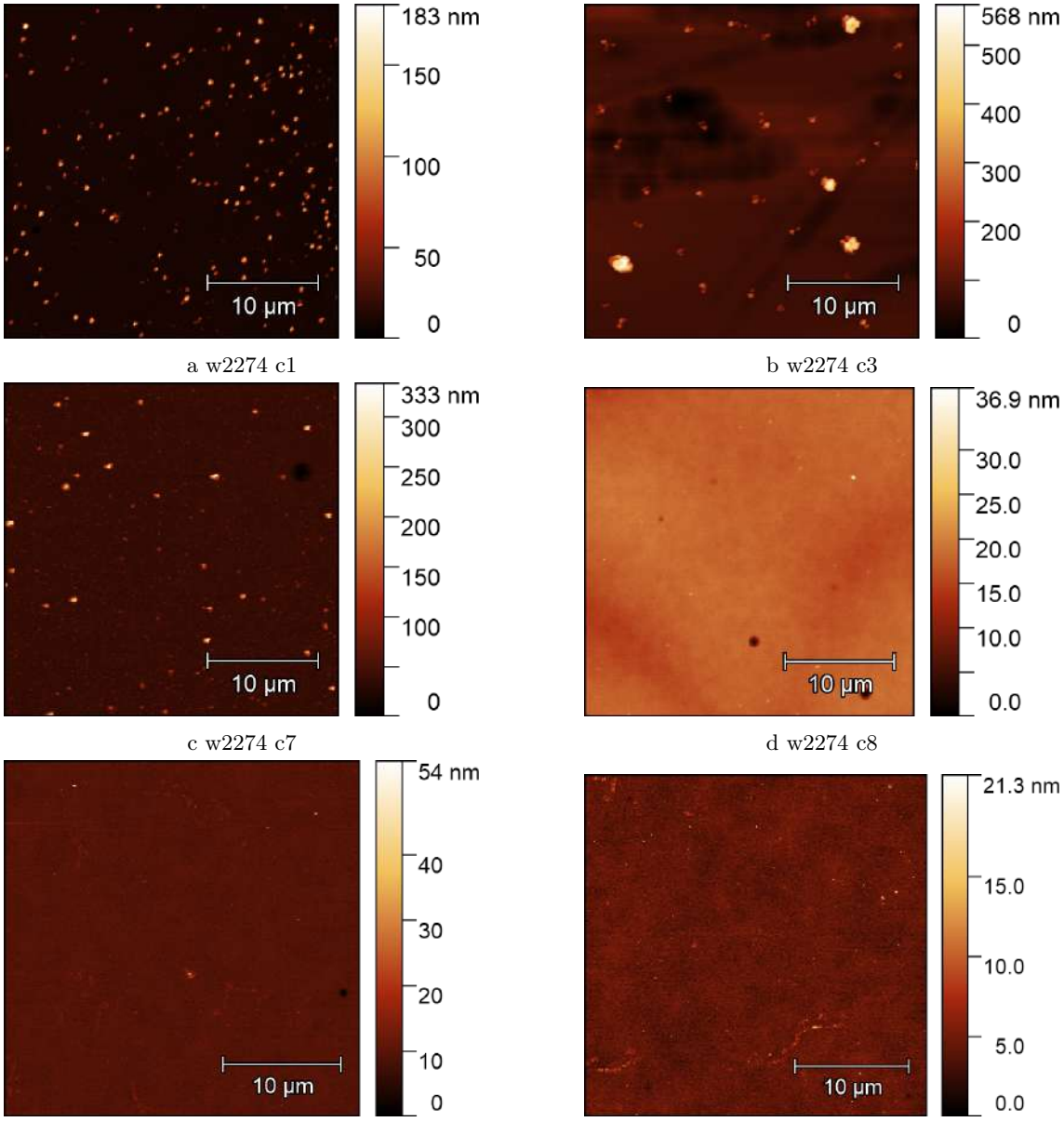

a w2274 c1 b w2274 c3

c w2274 c7 d w2274 c8

e w2275 c1 f w2275 c2

Figure A.1: Atomic force microscopy of a 30×30 μm^2 area near the apex of a dome on various chips after etching using the recipes presented in Table 3.1. The data is processed using analysis software Gwyddion by firstly removing a second-order polynomial background, and secondly aligning rows to remove AFM artefacts.

Bibliography

1. Chu, Y. *et al.* Creation and control of multi-phonon Fock states in a bulk acoustic-wave resonator. *Nature* **563,** 666–670. ISSN: 14764687 (Nov. 2018).
2. Von Lüpke, U. *et al.* Parity measurement in the strong dispersive regime of circuit quantum acoustodynamics. *Nature Physics* (2022).
3. Chu, Y. *et al.* Quantum acoustics with superconducting qubits. *Science* **358,** 199–202. ISSN: 10959203 (2017).
4. Bild, M. *et al.* Schrödinger cat states of a 16-microgram mechanical oscillator. *Science* **380,** 274–278. ISSN: 0036-8075 (Apr. 2023).
5. Chu, Y. & Gröblacher, S. A perspective on hybrid quantum opto- and electromechanical systems. http://arxiv.org/abs/2007.03360 (2020).
6. Bild, M. *Quantum acoustics for information processing and sensing* PhD thesis (2020), 1–16.
7. Von Lüpke, U., Rodrigues, I. C., Yang, Y., Fadel, M. & Chu, Y. Engineering phonon-phonon interactions in multimode circuit quantum acousto-dynamics. http://arxiv.org/abs/2303.00730 (2023).
8. Manenti, R. *et al.* Circuit quantum acoustodynamics with surface acoustic waves. www.nature.com/naturecommunications.
9. Satzinger, K. J. *et al.* Quantum control of surface acoustic-wave phonons. *Nature* **563,** 661–665. ISSN: 14764687 (Nov. 2018).
10. Malik, S., Jiang, W., Mayor, F. M., Makihara, T. & Safavi-Naeini, A. H. *Flexible Integration of Gigahertz Nanomechanical Resonators with a Superconducting Microwave Resonator using a Bonded Flip-Chip Method* 2023. arXiv: 2304.13592 [quant-ph].
11. Lauk, N. *et al.* Perspectives on quantum transduction. *Quantum Science and Technology* **5.** ISSN: 20589565 (2020).
12. Stannigel, K., Rabl, P., Sørensen, A. S., Zoller, P. & Lukin, M. D. Optomechanical transducers for long-distance quantum communication. *Physical Review Letters* **105,** 220501. ISSN: 00319007 (Nov. 2010).
13. Hann, C. T. *et al.* Hardware-efficient quantum random access memory with hybrid quantum acoustic systems. *Physical Review Letters* **123,** 250501. ISSN: 0031-9007 (Dec. 2019).
14. Jain, V. *et al.* Acoustic radiation from a superconducting qubit: From spontaneous emission to Rabi oscillations. http://arxiv.org/abs/2211.07475 (2022).
15. Cochrane, P. T., Milburn, G. J. & Munro, W. J. Macroscopically distinct quantum-superposition states as a bosonic code for amplitude damping. *Phys. Rev. A* **59,** 2631–2634. https://link.aps.org/doi/10.1103/PhysRevA.59.2631 (4 Apr. 1999).
16. Leghtas, Z. *et al.* Hardware-Efficient Autonomous Quantum Memory Protection. *Phys. Rev. Lett.* **111,** 120501. https://link.aps.org/doi/10.1103/PhysRevLett.111.120501 (12 Sept. 2013).
17. Gottesman, D., Kitaev, A. & Preskill, J. Encoding a qubit in an oscillator. *Physical Review A. Atomic, Molecular, and Optical Physics* **64,** 123101–1231021. ISSN: 10502947 (June 2001).

18. Laurent Michaud. *Coupling an acoustic resonator to a superconducting qubit using an improved flip-chip bonding process* tech. rep. (ETH Zurich, 2020).
19. Alessandro Bruno. *Parameter estimation for creating Schrödinger cat states in an electromechanical system* tech. rep. (ETH Zurich, 2022).
20. Banderier, H., Drimmer, M. & Chu, Y. Unified simulation methods for quantum acoustic devices. http://arxiv.org/abs/2301.05172 (2023).
21. Kharel, P. *et al.* Ultra-high- Q phononic resonators on-chip at cryogenic temperatures. *APL Photonics* **3,** 66101. ISSN: 23780967 (June 2018).
22. Pedro Rosso Gómez. *Engineering Eigenstates in High-Overtone Bulk Acoustic Resonators* tech. rep. (ETH Zurich, 2022).
23. Thomas Wilhelmus Johannus Palmen. *Grayscale Lithography For The Fabrication Of hbarBARs* tech. rep. (ETH Zürich, Zürich, Oct. 2021).
24. Pinto, R. M., Gund, V., Calaza, C., Nagaraja, K. K. & Vinayakumar, K. B. Piezoelectric aluminum nitride thin-films: A review of wet and dry etching techniques. *Microelectronic Engineering* **257,** 111753. ISSN: 0167-9317 (Mar. 2022).
25. Oxford Instruments. *Inductively Coupled Plasma Etching (ICP RIE)*
26. Von Lüpke, U. *et al. Flip chip technique for hybrid quantum systems* Poster presentation. Laboratory of Solid State Physics, ETH Zürich, 2021.
27. Anders, A. A structure zone diagram including plasma-based deposition and ion etching. *Thin Solid Films* **518,** 4087–4090. ISSN: 0040-6090. https://www.sciencedirect.com/science/article/pii/S0040609009018288 (2010).
28. Cho, H. *et al.* Inductively coupled plasma etching of III-nitrides in Cl2/Xe, Cl2/Ar and Cl2/He. *MRS Online Proceedings Library (OPL)* **537** (1998).
29. ANSYS, Inc. *ANSYS Electronic Desktop* https://www.ansys.com/. 2021.
30. Stefano Marti. *Optimization of phononic radiation loss patterns in a high overtone bulk acoustic resonator* tech. rep. (ETH Zurich, 2022).
31. Allresist. *7. Why may air bubbles develop in photoresist films, and how can they be avoided?* [Online; accessed 11-May-2023]. https://www.allresist.com/resist-wiki-why-may-air-bubbles-develop-in-photoresist-films-and-how-can-they-be-avoided/.
32. Dominique Collé. *Grayscale Lithography - Creating complex 2.5D structures in thick photoresist by direct laser writing* 2019. https://epic-events.eu/epic/2019/suss2019/191107_EPIC_SUSS2019_P45.pdf.
33. Kluyver, T. *et al. Jupyter Notebooks – a publishing format for reproducible computational workflows* in *Positioning and Power in Academic Publishing: Players, Agents and Agendas* (eds Loizides, F. & Schmidt, B.) (2016), 87–90.
34. MicroChemicals. *Technical datasheet AZ®4500 Series* 2023. https://www.microchemicals.com/micro/tds_az_4500_series.pdf.
35. EV Group. *EVG®620 NT Mask Alignment System User Manual* EV Group (2021).
36. Stoeckel, C. *et al.* Pulsed DC magnetron sputtered piezoelectric thin film aluminum nitride - Technology and piezoelectric properties. *Journal of Applied Physics* **116,** 34102. ISSN: 10897550. /aip/jap/article/116/3/034102/373870/Pulsed-DC-magnetron-sputtered-piezoelectric-thin (July 2014).
37. Gokhale, V. J. *et al.* Epitaxial bulk acoustic wave resonators as highly coherent multiphonon sources for quantum acoustodynamics. *Nature communications* **11,** 2314. ISSN: 20411723 (2020).